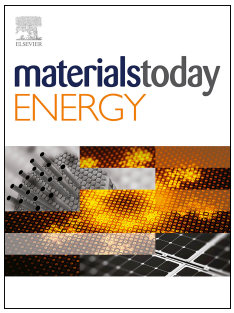

Slug flow synthesis of NCMA: Effect of substitution of cobalt with aluminum on the electrochemical performance of Ni-rich cathode for lithium-ion battery

Arjun Patel, Sourav Mallick, Jethrine H. Mugumya, Nicolás Lopez-Riveira, Sunuk Kim, Mo Jiang, Mariappan Parans Paranthaman, Michael L. Rasche, Herman Lopez, Ram B. Gupta

PII: S2468-6069(24)00057-1

DOI: https://doi.org/10.1016/j.mtener.2024.101545

Reference: MTENER 101545

To appear in: *Materials Today Energy*

Received Date: 28 November 2023

Revised Date: 9 February 2024

Accepted Date: 27 February 2024

Please cite this article as: A. Patel, S. Mallick, J.H. Mugumya, N. Lopez-Riveira, S. Kim, M. Jiang, M.P. Paranthaman, M.L. Rasche, H. Lopez, R.B. Gupta, Slug flow synthesis of NCMA: Effect of substitution of cobalt with aluminum on the electrochemical performance of Ni-rich cathode for lithium-ion battery, *Materials Today Energy*, https://doi.org/10.1016/j.mtener.2024.101545.

TOC

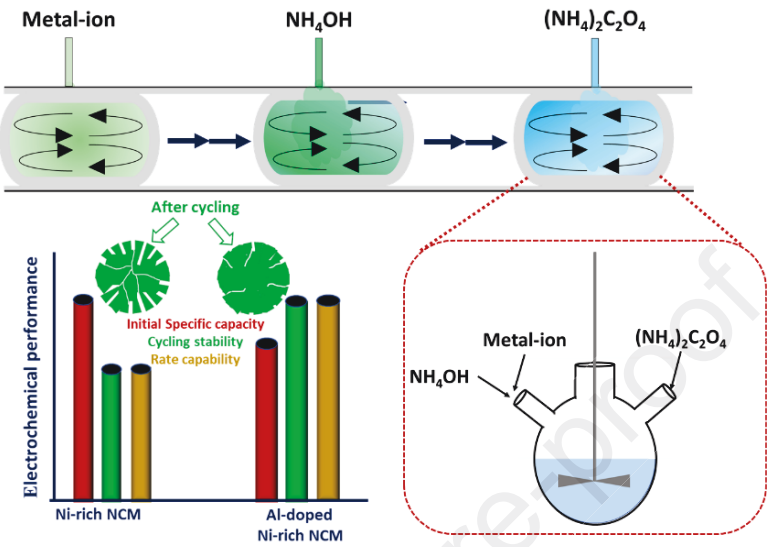

Slug flow synthesis of NCMA: Effect of substitution of cobalt with aluminum on the electrochemical performance of Ni-rich cathode for lithium-ion battery

Arjun Patel[1], Sourav Mallick[1], Jethrine H. Mugumya[1], Nicolás Lopez-Riveira[1], Sunuk Kim[1], Mo Jiang[1], Mariappan Parans Paranthaman[2], Michael L. Rasche[1], Herman Lopez[3], and Ram B. Gupta[1]*

[1]*Department of Chemical and Life Science Engineering, Virginia Commonwealth University, Richmond, VA, 23219, USA.*

[2]*Chemical Sciences Division, Oak Ridge National Laboratory, Oak Ridge, TN, 37831, USA*

[3]*Ionblox Inc., Fremont, CA, 94538, USA*

Abstract

Nickle-rich $Li[Ni_{1-x-y}Co_xMn_y]O_2$ ($x, y \leq 0.1$) (NCM) layered materials are known as promising cathode materials for next-generation lithium-ion batteries and electric vehicles owing to their high reversible capacity and high operating voltage of up to 3.6 vs Li/Li^+. However, issues, such as irreversible phase transition, cation mixing, microcrack formation, thermal and structural stability of the material prevent its widespread adoption. Although, cation doping is a well-known technique to enhance the electrochemical performance of the NCM-based cathode material, the performance of the material is very sensitive to the doping amount. In this study, three Al-doped quaternary Ni-rich cathode materials $Li[Ni_{0.85}Co_{(0.1-x)}Mn_{0.05}Al_x]O_2$ (where, x= 0 - 0.04) (NCMA) are synthesized through three-phase slug-flow based continuous manufacturing process followed by high temperature calcination to study the effect of Al-doping on the performance of the cathode material while reducing Co. The slug flow-based production platform has several advantages, like particle size uniformity, high production rate, and homogeneity in elemental distribution. It is found that with an increase in Al content, the specific capacity decreases but the cyclic stability and rate capability increases. Optimum Al-doping not only compensates for the adverse effect of low Co by decreasing the extent of cation mixing but also minimizes the electrode polarization and cracking of the particles.

Keywords: Ni-rich cathodes; Low-cobalt; Al-doped; Slug-flow process; controlled microstructure; NCMA; cycling stability.

1. Introduction

The economic and social prosperity of a nation largely depends on the successful production, storage and utilization of green and clean energy. Electrochemical energy storage devices, specifically Li-ion batteries (LIBs), a pioneering innovation by Noble laureates Professor John B. Goodenough, M. Stanley Whittingham, and Akira Yoshino, bring a revolution in the field of environment-benign energy storage technology and open up a new avenue to achieve a zero-carbon economy [1]. LIB market is further fueled by the aim to achieve the climate goals of the Paris Agreement, such as the replacement of conventional vehicles with electric vehicles (EV) [2]. LIBs with their high energy density and a longer cyclic life, make them a strong contender for powering EVs. Furthermore, the LIB market is motivated by the remarkable achievement of the application of 18650-type LIBs by Tesla Motors, delivering a driving range of 270 miles per charge [3]. However, a few of the intrinsic drawbacks of current LIB technology, including, high cost, lower specific capacity, and safety issues, hinder the growth of the LIB-based EV market. The fabrication cost as well as the charge storage performance of LIBs solely depends on the selection of its components, primarily on the cathode and anode active materials [4]. Graphite anodes, with a discharge capacity over 350 mAh g^{-1} is well complemented with EV energy requirement [5]. On the other hand, although lithium nickel cobalt manganese oxide (NCM)-based cathodes with an equal percentage of the three transition metals (NCM111) is well established for commercial application, high cost, and poor specific capacity (~150-160 mAh g^{-1}) limits the successful implementation of LIBs in the EV technology-like high energy applications [6]. Therefore, to achieve a satisfactory range of energy density and also to attenuate the cobalt-mining related socio-economic issues, scientific efforts are made towards developing various Ni-rich, Co-less cathode materials which can deliver a higher discharge capacity (~200 mAh g^{-1}) and high operation voltage (3.6 V vs Li/Li^{+}) compared to traditional $LiFePO_4$ (LFP and $LiCoO_2$ (LCO).

Among various Ni-rich cathode materials, lithium nickel cobalt manganese oxide ($LiNi_xCo_yMn_{1-x-y}O_2$ or NCM) and lithium nickel cobalt Aluminum oxide ($LiNi_xCo_yAl_{1-x-y}O_2$ or NCA) are potential candidates for EV battery applications due to their high capacity and higher operating voltage. [7] Although NCM materials are superior in terms of capacity and cycling at room temperature, NCA materials are better in terms of higher temperature cycling, safety, and cost [8–10]. However, an increase in Ni-content (> 0.8) in the layered oxide aggravates issues like, poor rate capability and short cycling performance due to the extensive

volume contraction/expansion during the phase change above 4.2 V vs. Li/Li^+ [11]. Initially, the microcracks are formed on the surface and then propagate towards the core of the secondary particles. The formation of Ni^{4+} at the highly charged state further accelerates the microcrack formation by reacting with the electrolyte [12]. Another, burning issue with Ni-rich and Co-less/free cathodes is high percentage of cation mixing. Notably, due to the lack of unpaired electrons in its e_g/t_{2g} level Co^{3+} does not undergo any kind of super-exchange interaction with neighboring Ni^{2+} and thus prevents the cation mixing in a large extent. In the absence of sufficient Co^{3+}, the mixing of cation will become highly facile during the heat treatment or upon potential induced cycling [13]. To mitigate these issues, researchers came up with the method of doping foreign metal-ions into the crystal moiety of the layered oxide-based materials, which largely modifies the local electronic environment of the crystal structure. The benefits of ion-doping are multidimensional, such as it improves the conductivity of the oxide-based materials, improves the Li^+ diffusion kinetics and prevent the cathode dissolution and mixing related issues [11]. Al^{3+} is one of the metal dopants commonly used to stabilize the layered structure of NCM. Al is known to improve the thermal stability of the material due to a stronger Al-O bond than (Ni, Co, Mn)-O bond [14–17]. Aluminum doping can effectively reduce the volume expansion and contraction during intercalation and deintercalation along with intrinsic mechanical strain and microcrack formation and progression [5]. Zhang et al. experimentally proved that, Al-doping is highly effective to decrease the electrode polarization upon cycling by preventing the H2-H3 phase transition in Ni-rich NCMs [18]. It also mitigates the surface degradation caused by the parasitic reaction of electrolytes and facilitates the Li^+ diffusion kinetics [11].

Another area to be improved for commercialization of cathode material includes the continuous manufacturing of the material. There are several methods used to synthesize cathode materials such as solid state, sol-gel, spray pyrolysis, solvothermal and co-precipitation [11,19]. Co-precipitation is most commonly employed method for synthesizing transition metal oxide precursors [11,19].These precursors can also be further classified into three subcategories based on the anion used for the precipitation process, namely hydroxide, carbonate and oxalate [20–22]. Hydroxide precursors are widely adopted due to an even distribution of transition metals (TM) and better tap density. However, the process is pH sensitive and can suffer from manganese oxidation. On the other hand, oxalate and carbonate routes are less prone to pH change and oxidation. However, carbonates can lead to poor control [23] over morphology and Ni-deficit precursors [24]. Oxalate precursors have an advantage of better control over

morphology, neutral pH around 7-8 and stability in air. On the other hand, the quality of product does not depend only on the chemical parameters but also depends on the type of reactor used. Spatial homogeneity in the reactor plays and important role in the quality of the product. Inhomogeneity in microenvironment in terms of temperature, concentration or degree of mixing throughout the reactor is one of the drawbacks of conventional batch reactors [25,26]. Semi-batch reactors are better than batch reactor in terms of control as it is an open system (has an inlet and /or outlet) and reactants are fed in continuously in a controlled environment. This is reason behind a widespread adoption of semi-batch systems in the battery and other industries [27,28]. However, semi-batch reactors are also prone to the spatial inhomogeneity as batch reactors. Slug flow reactors comes under the class of continuous tubular reactor and are known for a better control over the overall process and the quality of the product owning to its inherent properties like internal circulation and enhanced heat and mass transfer [29–31]. Slug flow can be categorized into two phase and three-phase slug flow systems. Two-phase slug flow systems, either gas-liquid or liquid-liquid, are most commonly reactors used in different industries [32,33]. The issue with these systems is fouling of the tubes, i.e. when a reactant or product with a high affinity towards the tubing surface is present in the system, it might stick to the wall and causes fouling. Reagent addition is also inaccurate in two phase slug-flow systems due to the formation of extra slugs while adding new reagent. Introducing a third phase is helpful to overcome the inaccuracies of the two-phase slug flow systems [34]. The immiscible third phase isolates the tubing surface and the reaction mixture. Mass transfer is also enhanced by using liquid-liquid-gas due to a reduced interfacial tension between two liquid phases [32]. Reagent addition is easier in the three-phase slug flow owing to the density difference of three phases, making slug flow versatile to any chemical process requiring multiple reagent addition [34].

Herein, we have utilized the three-phase slug-flow reactor system as a continuous manufacturing platform for NCMA based Ni-rich cathode material using oxalate co-precipitation chemistry. Three different $Li[Ni_{0.85}Co_{0.1-x}Mn_{0.05}Al_x]O_2$-based cathode materials are synthesized with same nickel (85 %) and manganese (5 %) content, but with different cobalt (10-6 %) and aluminum (0-4 %) content. Detailed physical characterizations and electrochemical analysis are performed to understand the effect of Co-substitution by Al in the crystal moiety of Ni-rich layered cathode. It was observed that, the cathode with 8 % Co and 2 % Al shows an improved electrochemical performance in terms of cycling stability, rate capability, Li^+ diffusion kinetics and surface stability.

2. Experimental section

2.1 Materials

Nickel(ii) sulfate hexahydrate (≥98%), manganese(ii) sulfate monohydrate (≥99%), cobalt(ii) sulfate heptahydrate (≥99%), ammonium oxalate (≥99%), ammonium hydroxide (28% NH_3 in H_2O, purity ≥99.99%), Aluminum sulfate ($Al_2(SO_4)_3.xH_2O$, light mineral oil and lithium hydroxide (≥98%) were purchased from Sigma-Aldrich. All chemicals were used as received without further treatment. All the solutions were prepared with deionized water.

2.2 Slug Flow Synthesis Platform

The schematic illustration of three-phase slug flow platform used for the synthesis of NCMA precursors is shown in Fig. 1a. The setup uses four syringe pumps (New era model #1000) to feed the reactants into a fluorinated ethylene propylene (FEP) tubular reactor with an internal diameter of 2.4 mm and a mass flow controller (Omega, model# FMA-2716A) to control nitrogen flowrate. A three-phase slug flow setup is designed as mention in our previous works. [35–37] To synthesize NCMA with different aluminum and cobalt content, stoichiometric amount of $NiSO_4.6H_2O$, $CoSO_4.7H_2O$, $MnSO_4.H_2O$ and $Al_2(SO_4)_3.xH_2O$ is dissolved in de-ionized water to prepare 0.5 M metal-ion solution. This solution is injected at the first T-mixer

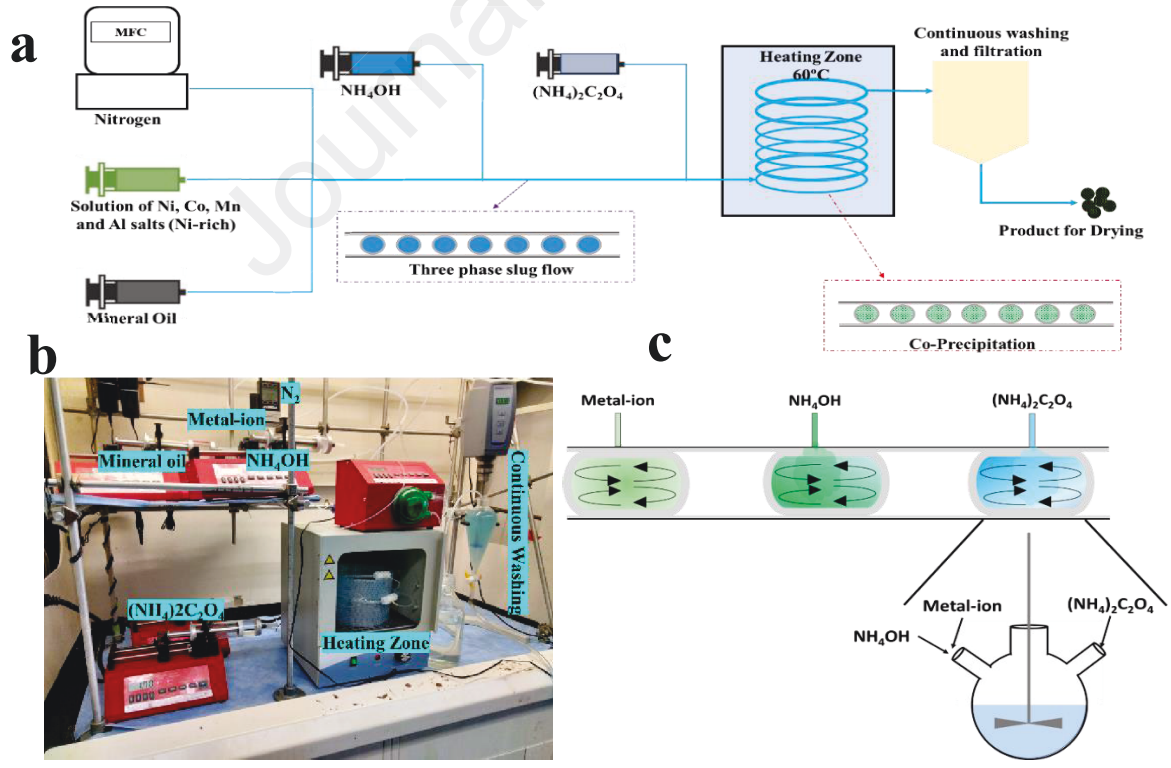

Fig. 1. (a) Schematic of slug flow setup, (b) a digital image of the slug flow setup and (c) representation of each slug as a micro-liter batch reactor.

with nitrogen and mineral oil to form three-phase slug flow. NH_4OH is then added to adjust the pH to 7.5 and to slow down the precipitation to control nucleation rate followed by ammonium oxalate addition to precipitate out the metal ions at 60°C. As these slugs move along the tubing the precursor particles grow in size. At the outlet of the tubular reactor, a 3000 ml quenching flask containing 1000 ml of deionized water is used to stop the reaction along with washing. The drain from the quenching flask is connected to a filtration unit to continuously wash and filter the precursor material. The volume of water in the quenching flask is maintained constant by adding fresh makeup deionized water. The product from filtration is then centrifuged to remove traces of mineral oil before drying it at 90°C in a vacuum oven for 12 hrs to get the precursors. The digital image of the slug-flow setup is set-up is shown in Fig. 1 b.

2.3 Lithiation of NCMA Oxalate

The dried product is then calcined by mixing $LiOH.H_2O$ with the precursor [Li: (Ni +Mn + Co + Al) = 1.05:1] and heating the mixture at 750 ^{0}C for 10 hrs. in oxygen environment using a slow ramp rate of 0.4 ^{o}C min^{-1}. The as-obtained black colored powder samples are then cooled down and crushed with mortar-pestle to get the NCMA-oxide with the molecular formula of $Li(Ni_{0.85}Co_{(0.1-x)}Mn_{0.05}Al_x)O_2$, where, x= 0 – 0.04) The three oxide materials are abbreviated as NCMA-(10,0), NCMA-(8,2) and NCMA-(6,4) based on Co and Al content (%) in the material.

2.4 Material Characterizations

The morphology and element distribution of the precursors and lithiated powders were checked with Scanning Electron Microscopy (SEM, SU-700, Hitachi) equipped with Energy Dispersive Spectroscopy (EDS) system. Thermogravimetry analysis were performed using TGA Q500 (TA instruments) at a ramp rate of 10°C min^{-1} in N_2 and O_2 environment. The crystalline form was determined by X-ray Powder Diffraction (PANalytical, Empyrean X-ray diffractometer) using Cu Kα ($\lambda = 1.5406$ Å) radiation source with a step of 0.02^o at 40 kV and 40 mA. Inductively coupled plasma-optical emission spectrometry (ICP-OES, Agilent Technologies, 5110-MS) was used to carry out compositional analysis of the material. X-ray Photoelectron spectroscopy (XPS) of the Al-doped lithiated material was performed using Phi VersaProbe III Scanning XPS Microprobe.

2.5 Electrochemical Measurements

The electrochemical tests were conducted using CR2032 type coin cells (MTI). Active material (NCMA), carbon black (super C65) and polyvinylidene difluoride (PVDF)(HSV900) in N-methyl pyrrolidone (NMP)(Sigma) [weight ratio of 8:1:1] were mixed to form a slurry and the slurry was coated on battery grade aluminum foil (MTI corp.) using a doctor blade. The electrodes were dried at 120 ^{0}C under vacuum for 12 hrs., rolled pressed and punched into 14 mm diameter round disks. The mass loading of the active material on the cathode was 9.0-10.0 mg cm^{-2}. The CR2032 coin cells were fabricated by placing the electrolyte-soaked Celgard 2340 Trilayer Microporous membrane (separator) in between the cathode (NCMA) and anode (lithium metal foil) inside an argon-filled glove box. 1.0 M $LiPF_6$ in ethylene carbonate/dimethyl carbonate (EC/DMC=1:1) was used as the electrolyte. The full cell LIB was made using the NCMA-(8,2) coated Al-foil as cathode and graphite coated Cu foil as anode. The loading of the two electrodes are adjusted by calculating the charge to mass ratio. The electrochemical performance of the cathode is evaluated through charge-discharge, rate capability and cycle life in MTI and ARBIN battery cycler considering 1C = 180 mA g^{-1}. The electrochemical impedance spectroscopy (EIS) was performed at various stages of cycling with an amplitude of 5 mV within a frequency range of 10^5 Hz to 10^{-2} Hz using a Gamry potentiostat Interface 5000E. All electrochemical tests were conducted at room temperature.

3. Results and Discussion

3.1 Slug flow parameters

In order to design three-phase slug flow reactors to produce NCMA precursors, it is important to study the formation mechanism of stable uniform slugs. The slug formation process for a single slug can be understood by four consecutive steps as (i) growth of the disperse phase and continuous phase; (ii) neck formation by the front section of the slug, which grows up to the boundary of the cross mixer; (iii) continuing growth of slug-volume by the combined effect of pressure build-up by three phases, the interfacial pressure of the neck and tip, and the shear force. While the slug moves downstream, the neck gets thinner, and finally (iv) collapse due to the disparity in dynamic equilibrium of forces, leading to the formation of slugs and flowing downstream [38–40]. Various parameters that affect the reactor efficiency, including flow rate, volume and concentration of the feeding solutions, residence time, number of feeding points, length and diameter of the tubular reactor, etc. must be investigated to design a three-phase slug flow reactor as a continuous co-precipitation platform. The properties such as, pressure drop, slug length, oil film thickness and slug velocity, are determined by the flowrate of each

fluid. If the flowrate of carrier phase(oil) is significantly less than the gas and metal ion solution (DI water), the reaction mixture-slugs will not be completely wrapped in the oil and precipitates grown inside these slugs may stick to the inner wall of the tubing, causing clogging and fouling related issues. On the other hand, when the oil flow rate is comparatively larger than metal ion solution, unstable and non-uniform oil slugs will form, leading to a failure in reagent addition [36,37]. The flow rate of each fluid should be determined according to the total concentration of the injected metal salt concentration. The tube length and flow rate combinedly determine the residence time, more precisely the reaction time which is critical to ensure complete reaction and achieve a better yield. Very shorter or larger tube length may cause incomplete or agglomerated product, respectively. Hence, proper trade-off between tube length and flow rates are essential for the growth of evenly spaced slugs, which experiences the same micro-environment. Each slug behaves as an individual micro-liter batch reactor with enhanced internal mixing for the co-precipitation synthesis of cathode precursors (Fig. 1c). The parameter used to achieve the ideal conditions of slug formation are given in table 1.

Table 1. Flow parameters used in Slug flow reactor.

Feed	Flowrate	Volume
Nitrogen	9.5 SCCM	--
Mineral Oil	0.7 ml min^{-1}	As required
Metal-salts	1.0 ml min^{-1}	50 ml
NH_4OH	1.2 ml min^{-1}	60 ml
$(NH_4)_2C_2O_4$	1.7 ml min^{-1}	85 ml

3.2 Characterization of precursors

The ICP-OES analysis confirms the formation of the NCMA precursors with the atomic percent of 10, 8 and 6 % of Co (Fig. S1). The Al content also varies accordingly 0, 2 and 4%. The Ni (85 %) and Mn (5 %) remain same for all the three materials. The SEM images of the precursor particles show that the nanosized cuboidal primary particles are agglomerated to form the spherical secondary particles in all the three cases (Fig. 2 a-f). The size of the secondary particles is within the range of 4-6 μm and is not affected by the variation of Al content. The EDAX elemental mapping shows the homogeneous distribution of all the elements in the NCMA with and without Al-doing (Fig. S2).

One interesting phenomenon was observed in the shape of the primary particle upon switching the feeding sequence of NH_4OH and $(NH_4)_2C_2O_4$. When NH_4OH was injected first,

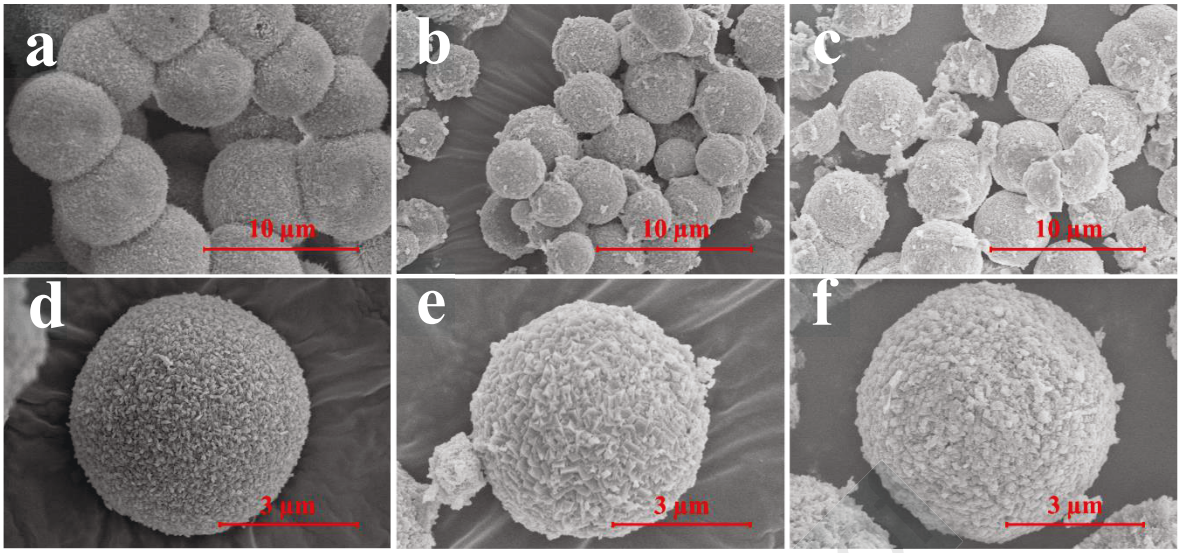

Fig. 2. SEM images for oxalate precursors of (a, d) NCMA-(10,0), (b, e) NCMA-(8,2), and (c, f) NCMA-(6,4).

the primary particles are cuboidal and densely packed (Fig. 2 and Fig. S3a). However, in the case of reverse order of feeding, the primary particles have flake-kind of morphology and loosely packed to form spherical secondary particle (Fig. S3b). In the former case the metal ions first make the complex with ammonia and then they are slowly released to form the oxalate precipitate, which allows them to stay longer time in solution and to grow three dimensionally (cuboidal). On the other hand, when the $(NH_4)_2C_2O_4$ was injected first, the metal-ions start to precipitate out from the solution promptly, leading towards flaky particles. It is a well-known fact that the, the densely packed cathode particles with higher tap density offer better electrochemical performance in terms of better structural integrity. [11] This is the reason of choosing the following feeding sequence in the slug-flow reactor: metal solution to NH_4OH to $(NH_4)_2C_2O_4$. According to the TGA profile, all the three precursors shows similar trend of losing surface-absorbed H_2O between 35-100 ^{0}C and crystal H_2O between 100-200 ^{0}C. TGA in N_2 environment shows that precursors with Al (2 and 4 atomic %) decomposed at around 300 ^{0}C, the precursor without Al decomposes at 350 ^{0}C. In the case of O_2 environment all three materials decomposes at 300 ^{0}C. Moreover, the weight loss for the precursor without Al is more than precursors with Al in both N_2 and O_2 environment (Fig. S4).

3.3 Characterization of the lithiated materials

The NCMA oxalate precursors are lithiated at a slow heating rate under a high oxygen flow environment (Fig. 3a). From the TGA analysis, it was observed that the transformation of metal-oxalate to metal oxide occurs by stepwise release of surface adsorbed water, crystal

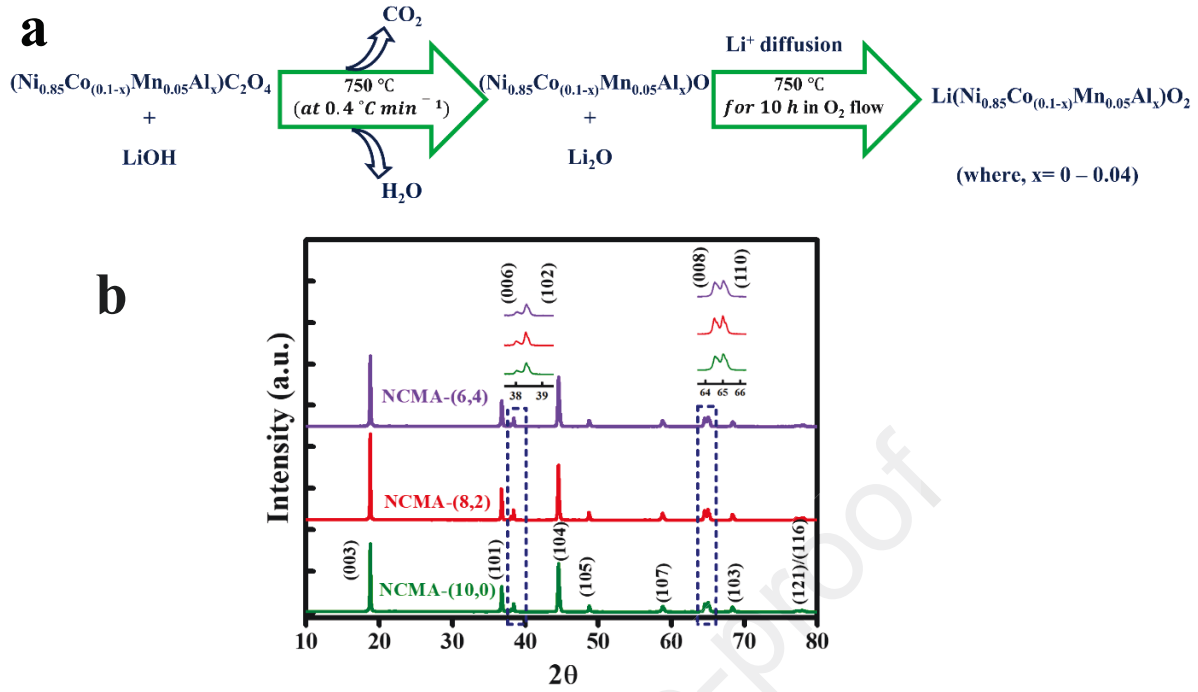

Fig. 3. (a) Lithiation condition of NCMA-ox precursors; (b) XRD profiles of (a) NCMA-(10,0), NCMA-(8,2), and NCMA-(6,4).

water and decomposition product like, CO_2. It is found that the spherical precursor particles were broken and become hollow when a higher heating rate is used for lithiation. This is due to a different rate of decomposition of oxalate to oxide and gas evolution at the core and the surface of the particles (Fig. S5). The slow heating rate ensures homogeneous heating throughout the secondary particles and retains its sphericity by preventing the abrupt structural change during the thermal decomposition of oxalate. The high oxygen flow is critically required to produce phase pure material by preventing the reduction of Ni^{3+} in the Ni-rich NCM [41]. The XRD profiles (Fig. 3b) of all the three NCMAs indicates the formation of phase-pure material with α-$NaFeO_2$ type structure belonging to the space group of (R-3m). The detail crystal parameters are obtained by Rietveld refinement (Fig. S6) and the data is shown in Table 2.

Table 2: Refinement data for XRD profiles for NCMA-(10,0), (8,2) and (6,4)

Sample	a & b (Å)	c (Å)	V ($Å^3$)	c/a	$I_{(003)}/I_{(104)}$	Ni^{2+} in Li layer (%)	Goodness of fit (R_{wp}/R_{exp})
NCMA-(10,0)	2.8651	14.178	100.79	4.948	1.42	2.6	1.76
NCMA-(8,2)	2.8665	14.188	100.96	4.949	1.55	2.18	1.63
NCMA-(6,4)	2.8654	14.185	100.86	4.951	1.43	2.5	1.67

The c/a ratios are calculated to be > 4.94 for all the three cases, indicating towards the well-defined hexagonal crystal structure. Formation of layered structure is further proved by the distinct splitting of (006)/(012) and (108)/(110) peaks (inset of Fig. 3b). It is observed that there is a slight increase in unit cell volume from NCMA-(10,0) to NCMA-(8,2) and then slight decrease for NCMA-(6,4). This anomaly in trend of volume change is due to the opposing effect of Co and Al-content in the structure. According to literature, the decreasing Co-content increases the lattice parameter values [42] and increasing Al-content leading towards contraction of lattice parameters [43]. Another interesting feature is observed in trend of $I_{(003)}/I_{(104)}$ ratio for the three materials. The highest value is observed for NCMA-(8,2) (1.55), whereas it is almost similar for NCMA-(10,0) and NCMA-(6,4) (1.42 and 1.43). The trend of $I_{(003)}/I_{(104)}$ ratio is well reflected to the percentage of cation mixing (Ni^{2+} in Li-layer), observed from the refinement data. The least cation mixing (2.18 %) is observed in case of NCMA-(8,2), whereas the mixing percentage is higher and close for the other two (NCMA-(10,0) = 2.6 % and NCMA-(6,4) = 2.5 %). In other way, although the NCMA-(6,4) contains the least amount of Co^{3+} (6 %), the cation mixing is almost close (slightly less) to the NCMA-(10,0), containing the highest Co^{3+} of 10 %. This trend strongly establishes the fact that, Al-doping effectively neutralizes the adverse effect of decreasing Co in the Ni-rich (Ni= 85%) NCM moiety by mitigating the cation mixing related issue. The NCMA-(8,2) contains the optimum percentage of Co (8%) and Al (2%) and shows the least cation mixing. The reduced cation mixing of the Al-substituted material can be attributed by the following two reasons- (i) the ionic radius of Al^{3+} (0.53Å) is significantly different compared to Li^+ radius (0.76 Å), (ii) Al^{3+} is a non-transition metal cation and it does not undergo super-exchange interaction with Ni^{3+}. From the SEM images (Fig. 4b, c, d), it is found that the secondary particles retain the sphericity for all

the three cases. The cross-sectional SEM images and the EDX mapping profiles are shown in Fig. S7. The EDX mapping proves the homogeneous distribution of all the elements throughout the particle. The particle size distribution plot for the three materials are shown in Fig. S8 and the secondary particle size for all the three materials are found to be within the range of 3-5 μm. After careful analysis of the SEM images, it is observed that the average value of primary particle size is smaller for Al-doped materials (NCMA-8,2 and 6,4) compared to undoped material. The smaller primary particles of Al-doped materials are densely packed and effectively relieve the internal strain during charge-discharge. In this context, it is worth mentioning that the NCMA materials are synthesized by oxalate co-precipitation followed by high temperature calcination. Hence, the primary and secondary particle size depend on various factors, such as NH_4OH concentration, metal ion composition and concentration, pH, calcination temperature and time. [11] In this work, the decreasing the Co^{3+} and incorporation of Al^{3+} into the reaction mixture simultaneously affecting the reaction kinetics and particle size.

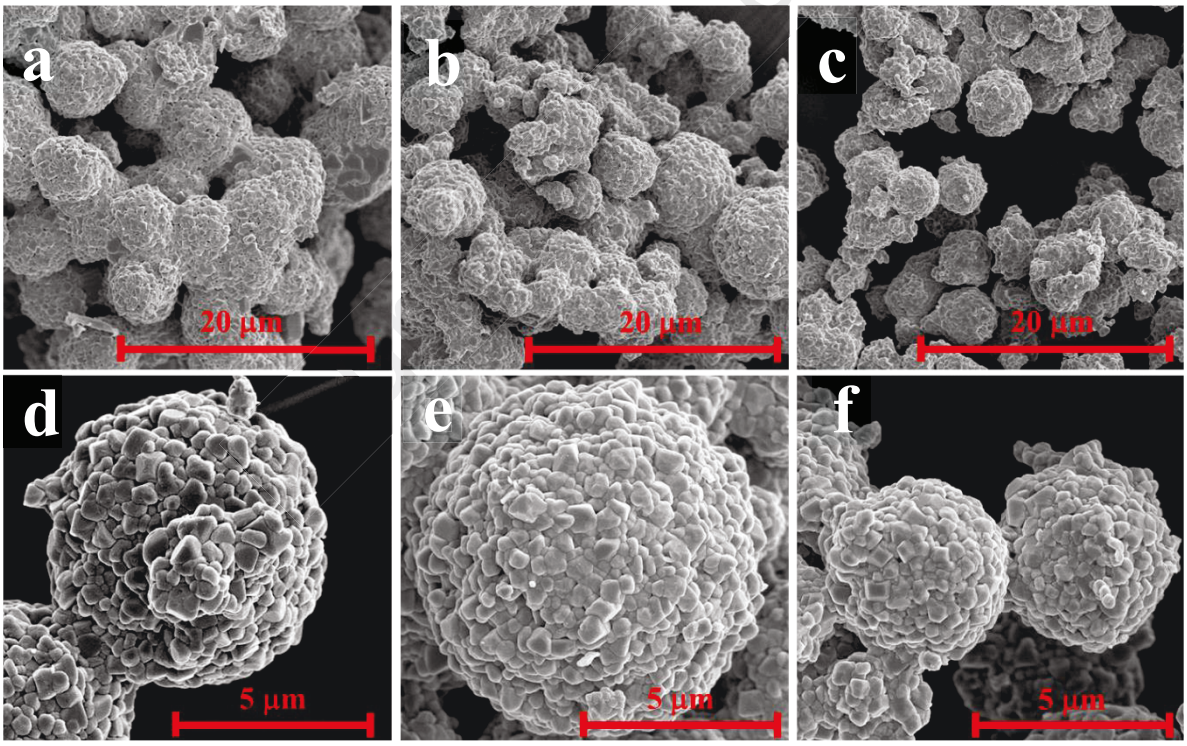

Fig. 4. SEM images show the surface morphology of the lithiated oxalates (a,d) NCMA-(10,0), (b,e) NCMA-(8,2), and (c,f) NCMA-(6,4) at different magnification

In order to understand the oxidation states of each element of NCMA, XPS analysis was performed with the Al-doped NCMA. From the survey scan (Fig. 5a) presence of all the elements, including Li, Ni, Co, Mn, Al and O are proved. The presence of C-peak indicates towards the formation of Li_2CO_3 based surface impurity during the high temperature calcination process [44]. The high-resolution Ni $2p_{3/2}$ peak is observed at 855.05 eV (Fig. 5b),

which can be deconvoluted in two peaks of 854.03 and 855.28 eV, corresponding to the Ni^{2+} and Ni^{3+} [45]. The peak at 861.25 eV is the satellite peak. It is observed from the deconvoluted Ni 2p XPS profile, that the relative Ni^{3+} percentage is approximately double to that of the Ni^{2+}, which effectively decreases the Ni^{2+}/Li^{+} mixing and offers improved cycling performance. The high-resolution Co $2p_{3/2}$ peak (Fig. 5c) at 779.4 eV signifies the presence of Co solely in +3 oxidation state [46]. Whereas, the deconvoluted Mn $2p_{3/2}$ spectra (Fig. 5d) is composed of Mn^{3+} and Mn^{4+} with a greater contribution from Mn^{4+}, which is common for Ni-rich NCM-based materials [46] The XPS profile of NCMA-(10,0) is shown in Fig. S9. In this case also, the Ni is found present in mixed valence of +2 and +3 (Fig. S9a). However, the peak position of Ni $2p_{3/2}$ is slightly lower (854.66 eV) compared to the Al-substituted material. Moreover, the Ni^{2+} content is also higher in case of Al-free material. This signifies that, the Al^{3+} doping effectively increases the Ni^{3+} in NCMA moiety to balance the charge. [47] The Co is present here in +3 state and Mn is observed in mix-valence of +4 and +3 (Fig S8 b and c).

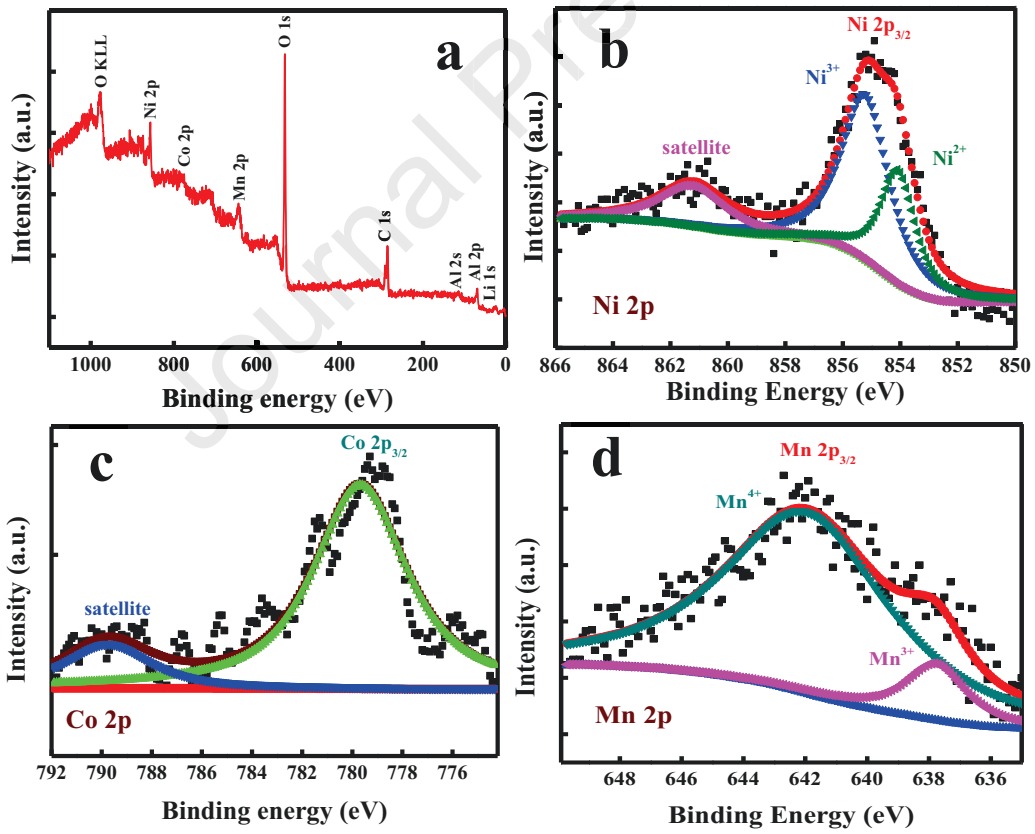

Fig. 5. XPS (a) survey scan and high-resolution profiles of (b) Ni 2p, (c) Co 2p, and (d) Mn 2p of Al-doped NCMA.

3.4 Electrochemical results

The electrochemical performance of three cathode materials are evaluated through the LIB coin cells (half-cell) within the voltage window of 2.8-4.3 V vs. Li/Li^+. From the charge discharge profiles at 0.1 C (Fig. 6a), it is observed that the specific capacity is gradually decreasing with increasing the Al content and decreasing the Co-content. The NCMA-(10,0) shows the highest specific capacity of 201 mAh g^{-1} and it decreased to 182 mAh g^{-1} for NCMA-(6,4). This decrease of specific capacity is common for Al-doped Ni-rich NCMs, which is attributed to the electrochemical inertness of the doped Al^{3+} [5,7,9,10,14–18]. The detail charge-discharge performance of all the three materials at different C-rates are provided in the Fig. S10. The initial charge discharge plots and the table for coulombic efficiency for the three materials are given in supporting information (Fig. S11 and Table S1). The rate capability plots (Fig. 6b) for the three materials are derived from the variation of the charge storage performance with varying C-rates. Comparing the rate capability of the three materials it is observed that, the NCMA-(8,2) shows a better rate capability up to 1 C by retaining 73 % of the specific capacity at 0.1 C (189 mAh g^{-1}). Whereas, NCMA-(10,0) and NCMA-(6,4) retained 57 and 64 %, respectively. The lesser Ni^{2+}/Li^+ mixing (observed from XRD) and facile Li^+ diffusion kinetics are the primary reasons of better rate capability for NCMA-(8,2). [48] Both the two Al-doped materials almost regain (~97%) its initial specific capacity when the charge discharge

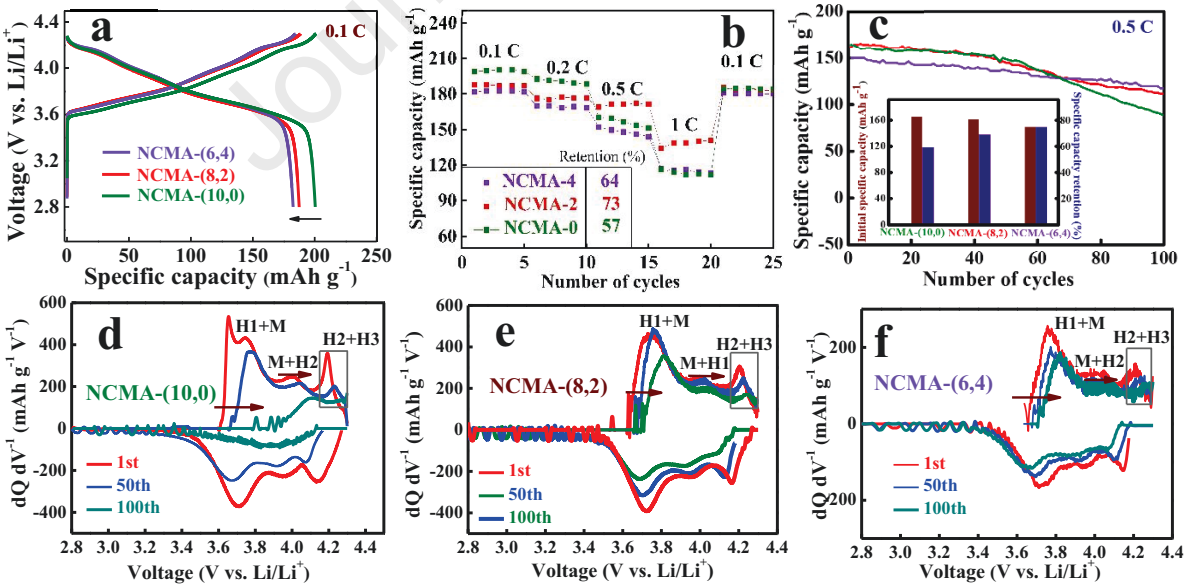

Fig. 6. Comparison of electrochemical performance of NCMA-(10,0), NCMA-(8,2) and NCMA-(6,4), in terms of (a) charge-discharge at 0.1 C; (b) rate capability and (c) cycling performance at 0.5 C. The dQ/dV profiles of (d) NCMA-(10,0), (e) NCMA-(8,2) and (f) NCMA-(6,4) are shown. The change in specific capacity retention (%) and initial specific capacity with change of composition is shown in the inset of (c).

performance was reperformed once again at 0.1 C; whereas, there is only 92% retention in case of NCMA-(10,0). The benefits of Al-doping are further realized through the improved cycling performance of the Ni-rich cathodes (Fig. 6c). The percent of specific capacity retention are 60, 70 and 77% for NCMA-(10,0), NCMA-(8,2) and NCMA-(6,4), respectively after 100 cycles at 0.5 C. Comparing the electrochemical performance it is observed that, with an increase in the Al content although the specific capacity is decreasing, the cycling stability is increasing (Fig. 6c inset). Among the three materials, the NCMA-(8,2)-based half-cell shows better electrochemical performance both in terms of cycling stability and rate capability. Hence, the material is selected to fabricate LIB-full cell combining with the graphite anode and the cycling performance was checked at 1 C for 100 cycles (Fig. S12). The NCMA-(8,2)-based full cell shows a very good cycling performance with a retention of 86% of its initial specific capacity with a coulombic efficiency of 99.5%.

In order to evaluate the reason behind the improved cycling stability upon increasing the Al-doping, the dQ/dV vs. V plots are derived at different stages of the cycling experiment, such as 2^{nd}, 50^{th} and 100^{th} for the three materials (Fig.6 d, e, f). As a general feature for Ni-rich NCM cathodes, three distinct redox pairs are observed in their dQ/dV profiles, corresponding to the stepwise phase transition from original layered hexagonal structure (H1) to monoclinic (M) to hexagonal 1 and 2 (H1 and H2) [18]. However, the polarization behavior of the cathodes upon cycling, in terms of peak shift and intensity variation are different in three materials. In the case of NCMA-(10,0), a huge shift of oxidation peaks towards higher voltage is observed from 2^{nd} to 50^{th} cycling and after 100^{th} cycle they shifted in more positive direction and merged together (Fig.6 d). Moreover, there is an abrupt change in the H2+H3 peak intensity upon cycling. The gradual change of overpotential and the sharp change in intensity of H2+H3 peak signifies the irreversibility of the electrochemical process, responsible for the severe anisotropic volume change, cracking and severe performance deterioration of the NCMA-(10,0) upon cycling. Although the polarization effect is also observed in the case of Al-doped materials, it become less severe with the increasing Al-content (Fig. 6 e,f). Specifically, the change in H2+H3 peak intensity become less prominent upon cycling for the Al-doped materials. This highly reversible nature of the phase transition assures good cycling stability for Al-doped material. The improved structural stability for Al-doped material can be attributed to the stronger Al-O bond compared to the bond between transition metal and oxygen. [14–17] A table based on the existing literature is included in the supporting information (Table S2), which shows that our study on substitution of Co with Al is a unique one and it successfully mitigates the issues for low-cobalt cathodes.

3.5 Electrochemical Impedance Spectroscopy

In order to get a better understanding on the co-relation between the decreasing Co-content and increasing Al-doping with Li-ion diffusion behavior in Ni-rich NCMs, electrochemical impedance spectroscopy (EIS) is performed at different stages of cycling for all three cathode materials. The Nyquist plots for NCMA-(10,0), (8,2) and (6,4) after 2nd, 50th and 100th cycles (at 0.5 C) are shown in Fig. 7a, b and c, respectively.

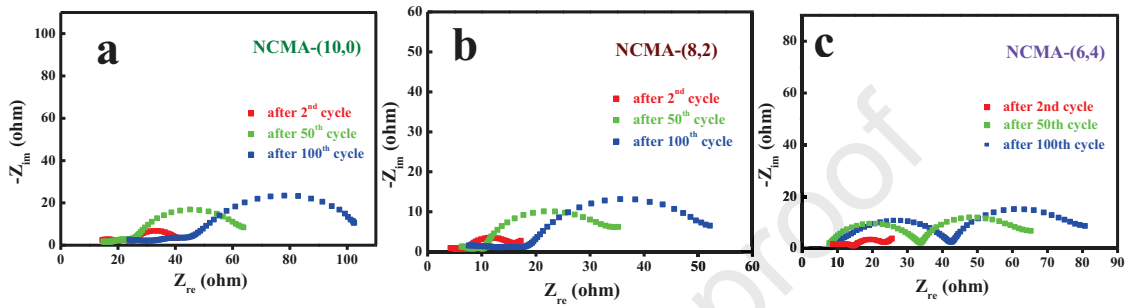

Fig. 7. Nyquist plots at different stages of cycling for (a) NCMA-(10,0); (b) NCMA-(8,2) and (c) NCMA-(6,4).

The plots are fitted with the suitable equivalent circuit, shown and described in Fig. S13. The change of surface phenomenon and charge-transfer properties upon cycling are tracked by R_f (surface resistance) and R_{ct} (charge-transfer resistance), respectively. On the other hand, the change of Li-ion diffusion kinetics is analyzed by W (Warburg impedance), the low frequency component of the impedance profile, which is related to the Li-ion diffusion coefficient (D_{Li+}) through the equation, given in supporting information. The trend of the change of R_f, R_{ct} and D_{Li+} for NCMA-(10,0), (8,2) and (6,4) are reported in the tabular form (Table 3.) and discussed accordingly.

Table 3: Data derived from impedance analysis for NCMA-(10,0), (8,2), (6,4).

Cathodes	2nd cycles	50th cycles	100th cycles
R_f (Ω) ± 0.04			
NCMA-(10,0)	3.11	6.86	11.83
NCMA-(8,2)	2.7	2.8	3.0
NCMA-(6,4)	4.77	5.5	9
R_{ct} (Ω) ± 3.0			
NCMA-(10,0)	11.87	25.15	63.64
NCMA-(8,2)	4.95	22.34	29.4
NCMA-(6,4)	6.5	26.76	34.53
D_{Li}+ x 10^{-12} (cm^2 s^{-1}) ± (2 x 10^{-14})			

NCMA-(10,0)	5.18	2.32	0.0127
NCMA-(8,2)	11.12	4.93	2.589
NCMA-(6,4)	5.39	4.89	2.45

Change in R_f: R_f (Ω) determines the ionic resistance of interface between the electrolyte and cathode surface. Ni-rich cathodes are severely affected by surface degradation and unwanted side reactions with electrolyte upon cycling. [11,49] The surface passivation/degradation is a combined result of (a) degradation of $LiPF_6$ and formation of acidic HF (b) oxidation of electrolyte solvent, such as EC and DMC, leading towards the formation of metal-organic films on the surface of NCM and (c) disintegration of primary particles, resulting in the cracking of the secondary particles. All of these issues increase the interfacial resistance, reflected through the R_f component. In our case, R_f is found to be increasing for all of the three materials with the progress of the cycling. However, lowest values of R_f are observed for NCMA-(8,2) at all the stages of cycling. In case of NCMA-(10,0), there is a ~4-fold increase of R_f from 2nd to 100th cycle, which is only ~1.5 fold for NCMA-(8,2). On the other hand, the higher values of R_f in NCMA-(6,4) compared to the NCMA-(8,2) can be ascribed to the fact that, the higher Al-content creates a thick coating layer on the surface of Ni-rich cathode, leading towards higher surface resistance [50]. However, in this case also the increase of R_f is ~1.88 fold after 100 cycles, which is lesser than Al-free material. The aforementioned trend of R_f signifies the less surface reactivity and high ionic conductivity of NCMA-(8,2) compared to the undoped and highly doped cathodes. This proves that, the optimum amount of Al-doping efficiently protects the surface of Ni-rich NCMs, without compromising the surface conductivity.

Change in R_{ct}: Formation of less-conducting NiO-based rock-salt phase and particle disintegration are the primary reasons behind increasing the R_{ct} in Ni-rich cathodes upon continuous cycling. In our case the three as-synthesized NCMA materials also show similar trend of gradual increasing of R_{ct}, but with different extent. NCMA-(10,0) shows the initial R_{ct} (after 2nd cycle) of 11.87 Ω increase to 25.15 Ω after 50th and finally to 63.64 Ω after 100th cycle. Whereas, for both the NCMA-(8,2) and NCMA-(6,4) the value of R_{ct} does not reach above the 35 Ω even after 100 cycle. This further indicates towards less polarization and improved structural integrity of the Al-doped cathode.

Change in D_{Li+}:

The Li^+ diffusion kinetics in Ni-rich NCM largely depends on the bulk structure of the cathode material and it varies with the progress of the charge discharge cycling. The change of Li^+ diffusion kinetics due to potential induced charge-discharge cycling is caused by the two major factors, (a) the extent of H2 to H3 phase transition at the higher voltage range during charging and (b) the degree of Ni^{2+}/Li^+ mixing at the lower voltage range during discharge step. [48,51] Both of the above phenomenon not only results in the structural/phase change in Ni-rich cathode but also hampers the Li^+ diffusion kinetics. In our case, the diffusion co-efficient is found to follow the usual decreasing trend upon cycling for all the three materials due to the increased mixing and phase change. However, NCMA-(8,2) achieves higher diffusion co-efficient values at each of the three stages of the cycling compared to other two materials. Better diffusion co-efficient for NCMA-(8,2) is a combined effect of decreased cation mixing (Table 2) and improved structural stability of the material (Fig. 8). On the other hand, NCMA-(10,0) and NCMA-(6,4) shows almost similar values of diffusion co-efficient at the beginning of the cycling, which is drastically decreased for the NCMA-(10,0) at the end of the 100 cycle. The percent of cation mixing is almost similar for the as-synthesized NCMA-(10,0) and NCMA-(6,4), ensures the similar diffusion behavior initially. However, the greater extent of electrode polarization caused by the drastic and irreversible phase transition (specially, H2 to H3) in NCMA-(10,0) leads to an abrupt deterioration of the Li^+ kinetics during further cycles.

3.6 Post-cycling analysis

Post-cycling SEM of the cathode was performed by de-crimping the coin cell after 100 cycles (0.5C) to understand the reason behind the difference in the cycling stability of the three materials. In the case of NCMA-(10,0), it is observed that the primary particles are disintegrated from the surface, leading towards the structural collapse of the secondary particles and poor cycling performance (Fig.8 a). However, for NCMA-(8,2) and NCMA-(6,4) the secondary particles retain its initial integrity upon cycling and ensures less performance decay (Fig.8 b and c). Cross-sectional SEM images (Fig. S14) further confirms the micro-crack formation in NCMA-(10,0) upon cycling. Whereas, no cracking is observed in case of NCMA-(8,2), signifies that the Al-doping effectively improves the structural robustness. [52,53] From the post cycling XRD (Fig. S15) and the refined data (Table 4), it is observed that the NCMA-(10,0) shows highest volume change after cycling, indicating towards more irreversibility in the H2-H3 phase transition, leading towards poor cycling performance. On the other hand, the Al-substituted materials shows lesser volume change and better cycling stability.

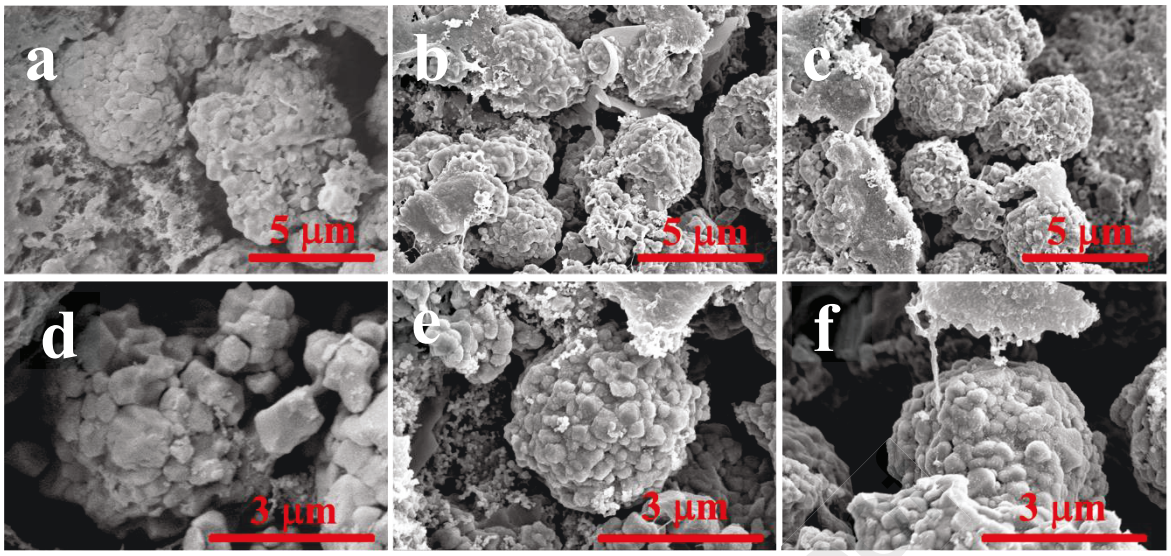

Fig. 8 Post-cycling SEM images of (a,d) NCMA-(10,0), (b,e) NCMA-(8,2) and (c,f) NCMA-(6,4). Disintegration of the primary particles are observed in NCMA-(10,0) after cycling.

Table 4. Refinement data of Post-cycling XRD.

Material	a(Å)	b(Å)	c(Å)	Volume(Å^3)
NCMA-(10,0)	2.83766	2.83766	14.41262	100.5063
NCMA-(6,4)	2.8538	2.8538	14.29198	100.8025
NCMA-(8,2)	2.86177	2.86177	14.25916	101.1334

4 Conclusion

In this work, we have demonstrated the continuous co-precipitation production of Ni-rich NCMA cathode precursors with varying Co and Al content through three phase slug-flow manufacturing platform for the first time. The superiority of the process compared to the traditional stirred-tank reactor-based batch/semi-batch process lies on the fact that, scalable production is possible without compromising quality of the particle properties, such as size, morphology and chemical composition. The detailed description of the unique production process is included in the first part of the manuscript. Then, the as-synthesized oxalate precursors were lithiated at a high temperature with a slow heating rate under oxygen flow to get the final cathode materials, abbreviated as NCMA-(10,0), NCMA-(8,2) and NCMA-(6,4). These materials were utilized to study the effect of gradual Co-substitution with Al on the structural parameters and electrochemical performance of the Ni-rich NCM (with 85% Ni). The trend of change in lattice parameters and cation mixing were evaluated by the refinement

of the XRD data. Least cation mixing was observed for the NCMA-(8,2) (with, Co= 8% and Al= 2%), which further ensures the superior rate capability and Li^+ diffusion kinetics of the material. It was observed that, the initial capacity decreases with increasing amount of electrochemically inert Al in the NCMA structure. Whereas, optimum Al-doping (~2 %) efficiently decreases the adverse effects of decreasing Co by (i) reducing cation mixing; (ii) improving rate capability; (iii) decreasing polarization of electrodes; (iv) increasing capacity retention upon cycling and (v) retaining the structural integrity of the cathode during cycling.

CRediT authorship contribution statement

Arjun Patel: Methodology of material synthesis, investigation, software, data curation, writing - original draft, reviewing, validation. **Sourav Mallick:** Methodology and conceptualization of electrochemical experiments and analysis, writing- electrochemistry part, data-curation, validation**,** reviewing the manuscript. **Jethrine H. Mugumya and Nicolás Lopez-Riveira:** Assisted in synthesis. **Sunuk Kim:** Performed the TGA analysis. **Michael L. Rasche:** Worked on a theoretical model to improve the slug flow product quality. **Herman Lopez:** Helped with the experimental design. **Mo Jiang, Mariappan Parans Paranthaman, Ram B. Gupta:** Conceptualization, supervision and funding-acquisition.

All authors contributed to and approved the final version of the manuscript.

Declaration of competing interest

The authors declare no competing financial interest.

Acknowledgement

This material is based upon work supported by Virginia Commonwealth University and the National Science Foundation (Grant No. CMMI-1940948) and U.S. Department of Energy, Office of Energy Efficiency and Renewable Energy, Advanced Materials and Manufacturing Technologies Office (award DE-EE0009110)**.** Research conducted at ORNL was supported by the U.S. Department of Energy, Office of Energy Efficiency and Renewable Energy, Advanced Manufacturing Office. This manuscript has been authored by UTBattelle, LLC, under Contract No. DEAC05-00OR22725 with the U.S. Department of Energy. The U.S. Government retains and the publisher, by accepting the article for publication, acknowledges that the U.S. Government retains a nonexclusive, paid-up, irrevocable, worldwide license to publish or reproduce the published form of this manuscript, or allow others to do so, for U.S. Government purposes. The Department of Energy will provide public access to these results of federally sponsored research in accordance with the DOE Public Access Plan (http://energy.gov/downloads/doe-public-access-plan). Mingyao Mou and Sophie Kothie are acknowledged for providing the slug flow co-precipitation technology developed in Mo Jiang Lab.

References

[1] The Nobel Prize in Chemistry 2019. NobelPrize.org. Nobel Prize Outreach AB 2023. Tue. 6 Jun 2023. <https://www.nobelprize.org/prizes/chemistry/2019/summary/>, (n.d.).

[2] United Nations, Paris Declaration on Electro-Mobility and Climate Change & Call to Action, https://unfccc.int/news/the-paris-declaration-on-electro-mobility-and-climate-change-and-call-to-action, (n.d.).

[3] W. Yan, S. Yang, Y. Huang, Y. Yang, Guohui Yuan, A review on doping/coating of nickel-rich cathode materials for lithium-ion batteries, J. Alloys Compd. 819 (2020). https://doi.org/10.1016/j.jallcom.2019.153048.

[4] P.A. Nelson, S. Ahmed, K.G. Gallagher, D.W. Dees, Modeling the Performance and Cost of Lithium-Ion Batteries for Electric-Drive Vehicles, Third Edition, United States, 2019. https://doi.org/10.2172/1503280.

[5] W. Yan, X. Jia, S. Yang, Y. Huang, Y. Yang, G. Yuan, Synthesis of Single Crystal $LiNi_{0.92}Co_{0.06}Mn_{0.01}Al_{0.01}O_2$ Cathode Materials with Superior Electrochemical Performance for Lithium Ion Batteries, J. Electrochem. Soc. 167 (2020) 120514. https://doi.org/10.1149/1945-7111/abacea.

[6] J.H. Mugumya, M.L. Rasche, R.F. Rafferty, A. Patel, S. Mallick, M. Mou, J.A. Bobb, R.B. Gupta, M. Jiang, Synthesis and Theoretical Modeling of Suitable Co-precipitation Conditions for Producing NMC111 Cathode Material for Lithium-Ion Batteries, Energy & Fuels 36 (2022) 12261–12270. https://doi.org/10.1021/acs.energyfuels.2c01805.

[7] N. Muralidharan, E.C. Self, M. Dixit, Z. Du, R. Essehli, R. Amin, J. Nanda, I. Belharouak, Next-Generation Cobalt-Free Cathodes – A Prospective Solution to the Battery Industry's Cobalt Problem, Adv. Energy Mater. 12 (2022). https://doi.org/10.1002/aenm.202103050.

[8] S.-T. Myung, F. Maglia, K.-J. Park, C.S. Yoon, P. Lamp, S.-J. Kim, Y.-K. Sun, Nickel-Rich Layered Cathode Materials for Automotive Lithium-Ion Batteries: Achievements and Perspectives, ACS Energy Lett. 2 (2017) 196–223. https://doi.org/10.1021/acsenergylett.6b00594.

[9] U.H. Kim, L.Y. Kuo, P. Kaghazchi, C.S. Yoon, Y.K. Sun, Quaternary Layered Ni-Rich NCMA Cathode for Lithium-Ion Batteries, ACS. Energy Lett. 4 (2019) 576–582. https://doi.org/10.1021/acsenergylett.8b02499.

[10] W. Li, X. Liu, H. Celio, P. Smith, A. Dolocan, M. Chi, A. Manthiram, Mn versus Al in Layered Oxide Cathodes in Lithium-Ion Batteries: A Comprehensive Evaluation on Long-Term Cyclability, Adv. Energy. Mater. 8 (2018). https://doi.org/10.1002/aenm.201703154.

[11] S. Mallick, A. Patel, X.-G. Sun, M.P. Paranthaman, M. Mou, J.H. Mugumya, M. Jiang, M.L. Rasche, H. Lopez, R.B. Gupta, Low-cobalt active cathode materials for high-performance lithium-ion batteries: synthesis and performance enhancement methods, J. Mater. Chem. A 11 (2023) 3789–3821. https://doi.org/10.1039/D2TA08251A.

[12] H.-H. Ryu, K.-J. Park, C.S. Yoon, Y.-K. Sun, Capacity Fading of Ni-Rich $Li[Ni_xCo_yMn_{1-x-y}]O_2$ ($0.6 \leq x \leq 0.95$) Cathodes for High-Energy-Density Lithium-Ion Batteries: Bulk or Surface Degradation?, Chem. Mater. 30 (2018) 1155–1163. https://doi.org/10.1021/acs.chemmater.7b05269.

[13] J. Zheng, G. Teng, C. Xin, Z. Zhuo, J. Liu, Q. Li, Z. Hu, M. Xu, S. Yan, W. Yang, F. Pan, Role of Superexchange Interaction on Tuning of Ni/Li Disordering in Layered $Li(Ni_xMn_yCo_z)O_2$, J. Phys. Chem. Lett. 8 (2017) 5537–5542. https://doi.org/10.1021/acs.jpclett.7b02498.

[14] F. Zhou, X. Zhao, Z. Lu, J. Jiang, J.R. Dahn, The effect of Al substitution on the reactivity of delithiated $LiNi_{1/3}Mn_{1/3}Co_{(1/3-z)}Al_zO_2$ with non-aqueous electrolyte, Electrochem. Commun. 10 (2008) 1168–1171. https://doi.org/https://doi.org/10.1016/j.elecom.2008.05.036.

[15] S.-W. Woo, S.-T. Myung, H. Bang, D.-W. Kim, Y.-K. Sun, Improvement of electrochemical and thermal properties of $Li[Ni_{0.8}Co_{0.1}Mn_{0.1}]O_2$ positive electrode materials by multiple metal (Al, Mg) substitution, Electrochim. Acta 54 (2009) 3851–3856. https://doi.org/https://doi.org/10.1016/j.electacta.2009.01.048.

[16] J. Wilcox, S. Patoux, M. Doeff, Structure and Electrochemistry of $LiNi_{1/3}Co_{1/3-y}M_yMn_{1/3}O_2$ (M=Ti, Al, Fe) Positive Electrode Materials, J. Electrochem. Soc. 156 (2009) A192-A198. DOI 10.1149/1.3056109.

[17] U.-H. Kim, S.-T. Myung, C.S. Yoon, Y.-K. Sun, Extending the Battery Life Using an Al-Doped $Li[Ni_{0.76}Co_{0.09}Mn_{0.15}]O_2$ Cathode with Concentration Gradients for Lithium Ion Batteries, ACS Energy Lett. 2 (2017) 1848–1854. https://doi.org/10.1021/acsenergylett.7b00613.

[18] C. Zhang, J. Wan, Y. Li, S. Zheng, K. Zhou, D. Wang, D. Wang, C. Hong, Z. Gong, Y. Yang, Restraining the polarization increase of Ni-rich and low-Co cathodes upon cycling by Al-doping, J. Mater. Chem. A 8 (2020) 6893–6901. https://doi.org/10.1039/d0ta00260g.

[19] L. Xu, F. Zhou, B. Liu, H. Zhou, Q. Zhang, J. Kong, Q. Wang, Progress in Preparation and Modification of $LiNi_{0.6}Mn_{0.2}Co_{0.2}O_2$ Cathode Material for High Energy Density Li-Ion Batteries, Int. J. Electrochem. 2018 (2018) 6930386. https://doi.org/10.1155/2018/6930386.

[20] F. Schipper, E.M. Erickson, C. Erk, J.-Y. Shin, F.F. Chesneau, D. Aurbach, Review—Recent Advances and Remaining Challenges for Lithium Ion Battery Cathodes, J. Electrochem. Soc. 164 (2017) A6220–A6228. https://doi.org/10.1149/2.0351701jes.

[21] H. Dong, G.M. Koenig, A review on synthesis and engineering of crystal precursors produced: Via coprecipitation for multicomponent lithium-ion battery cathode materials, CrystEngComm 22 (2020) 1514–1530. https://doi.org/10.1039/c9ce00679f.

[22] M. Malik, K.H. Chan, G. Azimi, Review on the synthesis of $LiNi_xMn_yCo_{1-x-y}O_2$ (NMC) cathodes for lithium-ion batteries, Mater. Today Energy 28 (2022) 101066. https://doi.org/https://doi.org/10.1016/j.mtener.2022.101066.

[23] Z. Xu, L. Xiao, F. Wang, K. Wu, L. Zhao, M.-R. Li, H.-L. Zhang, Q. Wu, J. Wang, Effects of precursor, synthesis time and synthesis temperature on the physical and electrochemical properties of $Li(Ni_{1-x-y}Co_xMn_y)O_2$ cathode materials, J. Power Sources 248 (2014) 180–189. https://doi.org/https://doi.org/10.1016/j.jpowsour.2013.09.064.

[24] G.M. Jr. Koenig, I. Belharouak, H. Deng, Y.-K. Sun, K. Amine, Composition-Tailored Synthesis of Gradient Transition Metal Precursor Particles for Lithium-Ion Battery Cathode Materials, Chem. Mater. 23 (2011) 1954–1963. https://doi.org/10.1021/cm200058c.

[25] J. Jiang, H. Wu, L. Ni, M. Zou, CFD simulation to study batch reactor thermal runaway behavior based on esterification reaction, Process Saf. Environ. Prot. 120 (2018) 87–96. https://doi.org/https://doi.org/10.1016/j.psep.2018.08.029.

[26] L. Gutierrez, L. Gomez, S. Irusta, M. Arruebo, J. Santamaria, Comparative study of the synthesis of silica nanoparticles in micromixer–microreactor and batch reactor systems, Chem. Eng. J. 171 (2011) 674–683. https://doi.org/https://doi.org/10.1016/j.cej.2011.05.019.

[27] N. Ngoepe, A. Gutierrez, P. Barai, J. Chen, P. E. Ngoepe, J. R. Croy, The effects of process parameters on the properties of manganese-rich carbonate precursors: A study of co-precipitation synthesis using semi-batch reactors, Chem. Eng. Sci. 241 (2021) 116694. https://doi.org/https://doi.org/10.1016/j.ces.2021.116694.

[28] W. E, J. Cheng, C. Yang, Z. Mao, Experimental study by online measurement of the precipitation of nickel hydroxide: Effects of operating conditions, Chin. J. Chem. Eng. 23 (2015) 860–867. https://doi.org/https://doi.org/10.1016/j.cjche.2014.04.004.

[29] M. Jiang, Z. Zhu, E. Jimenez, C. D. Papageorgiou, J. Waetzig, A. Hardy, M. Langston, R.D. Braatz, Continuous-flow tubular crystallization in slugs spontaneously induced by hydrodynamics, Cryst. Growth Des. 14 (2014) 851–860. https://doi.org/10.1021/cg401715e.

[30] M. Mou, M. Jiang, Fast Continuous Non-Seeded Cooling Crystallization of Glycine in Slug Flow: Pure α-Form Crystals with Narrow Size Distribution, J. Pharm. Inno.v 15 (2020) 281–294. https://doi.org/10.1007/s12247-020-09438-0.

[31] Z. Chen, J. Xu, Y. Wang, Gas-liquid-liquid multiphase flow in microfluidic systems – A review, Chem. Eng. Sci. 202 (2019) 1–14. https://doi.org/https://doi.org/10.1016/j.ces.2019.03.016.

[32] M. Su, Y. Gao, Air–Liquid Segmented Continuous Crystallization Process Optimization of the Flow Field, Growth Rate, and Size Distribution of Crystals, Ind. Eng. Chem. Res. 57 (2018) 3781–3791. https://doi.org/10.1021/acs.iecr.7b05236.

[33] R. Antony, M. S. Giri Nandagopal, N. Sreekumar, S. Rangabhashiyam, N. Selvaraju, Liquid-liquid slug flow in a microchannel reactor and its mass transfer properties - A

review, Bull. Chem. React. Eng. Catal. 9 (2014) 207–223. https://doi.org/10.9767/bcrec.9.3.6977.207-223.

[34] A.M. Nightingale, T.W. Phillips, J.H. Bannock, J.C. de Mello, Controlled multistep synthesis in a three-phase droplet reactor, Nat. Commun. 5 (2014) 3777. https://doi.org/10.1038/ncomms4777.

[35] M. Mou, A. Patel, S. Mallick, K. Jayanthi, X.-G. Sun, M. Parans Paranthaman, S. Kothe, E. Baral, S. Saleh, J. H. Mugumya, M. L. Rasche, R. B. Gupta, H. Lopez, M. Jiang, Slug Flow Coprecipitation Synthesis of Uniformly-Sized Oxalate Precursor Microparticles for Improved Reproducibility and Tap Density of $Li(Ni_{0.8}Co_{0.1}Mn_{0.1})O_2$ Cathode Materials, ACS Appl. Energy Mater. 6 (2023) 3213–3224. https://doi.org/10.1021/acsaem.2c03563.

[36] M. Mou, A. Patel, S. Mallick, B. P. Thapaliya, M. P. Paranthaman, J. H. Mugumya, M. L. Rasche, R. B. Gupta, S. Saleh, S. Kothe, E. Baral, G. P. Pandey, H. Lopez, M. Jiang, Scalable Advanced $Li(Ni_{0.8}Co_{0.1}Mn_{0.1})O_2$ Cathode Materials from a Slug Flow Continuous Process, ACS Omega 7 (2022) 42408–42417. https://doi.org/10.1021/acsomega.2c05521.

[37] R. B. Gupta, M. Jiang, M. Mou, A. Patel, J. H. Mugumya, S. Mallick, H. Lopez, M. Paranthaman, (Invited) Slug-Flow Manufacturing of Nickel-Cobalt-Manganese-Oxide Cathode Particles for Lithium-Ion Batteries, ECS Meeting Abstracts MA2022-02 (2022) 25. https://doi.org/10.1149/MA2022-02125mtgabs.

[38] M. Jiang, R.D. Braatz, Low-Cost Noninvasive Real-Time Imaging for Tubular Continuous-Flow Crystallization, Chem. Eng. Technol. 41 (2018) 143–148. https://doi.org/https://doi.org/10.1002/ceat.201600276.

[39] M. Jiang, R.D. Braatz, Designs of continuous-flow pharmaceutical crystallizers: developments and practice, CrystEngComm 21 (2019) 3534–3551. https://doi.org/10.1039/C8CE00042E.

[40] M. L. Rasche, M. Jiang, R. D. Braatz, Mathematical modeling and optimal design of multi-stage slug-flow crystallization, Comput. Chem. Eng. 95 (2016) 240–248. https://doi.org/https://doi.org/10.1016/j.compchemeng.2016.09.010.

[41] J. Yuan, J. Wen, J. Zhang, D. Chen, D. Zhang, Influence of calcination atmosphere on structure and electrochemical behavior of $LiNi_{0.6}Co_{0.2}Mn_{0.2}O_2$ cathode material for lithium-ion batteries, Electrochim. Acta 230 (2017) 116–122. https://doi.org/https://doi.org/10.1016/j.electacta.2017.01.102.

[42] M. Bianchini, M. Roca-Ayats, P. Hartmann, T. Brezesinski, J. Janek, There and Back Again—The Journey of $LiNiO_2$ as a Cathode Active Material, Angew. Chem. Int. Ed. 58 (2019) 10434–10458. https://doi.org/https://doi.org/10.1002/anie.201812472.

[43] M. Guilmard, A. Rougier, M. Grüne, L. Croguennec, C. Delmas, Effects of aluminum on the structural and electrochemical properties of $LiNiO_2$, J. Power Sources 115 (2003) 305–314. https://doi.org/https://doi.org/10.1016/S0378-7753(03)00012-0.

[44] Z. Fang, M.P. Confer, Y. Wang, Q. Wang, M.R. Kunz, E.J. Dufek, B. Liaw, T.M. Klein, D.A. Dixon, R. Fushimi, Formation of Surface Impurities on Lithium–Nickel–Manganese–Cobalt Oxides in the Presence of CO_2 and H_2O, J. Am. Chem. Soc. 143 (2021) 10261–10274. https://doi.org/10.1021/jacs.1c03812.

[45] A.P. Grosvenor, M.C. Biesinger, R.St.C. Smart, N.S. McIntyre, New interpretations of XPS spectra of nickel metal and oxides, Surf. Sci. 600 (2006) 1771–1779. https://doi.org/https://doi.org/10.1016/j.susc.2006.01.041.

[46] G. Cherkashinin, K. Nikolowski, H. Ehrenberg, S. Jacke, L. Dimesso, W. Jaegermann, The stability of the SEI layer, surface composition and the oxidation state of transition metals at the electrolyte–cathode interface impacted by the electrochemical cycling: X-ray photoelectron spectroscopy investigation, Phys. Chem. Chem. Phys. 14 (2012) 12321–12331. https://doi.org/10.1039/C2CP41134B.

[47] Y.C. Li, W. Xiang, Z.G. Wu, C.L. Xu, Y. Di Xu, Y. Xiao, Z.G. Yang, C.J. Wu, G.P. Lv, X.D. Guo, Construction of homogeneously Al^{3+} doped Ni rich Ni-Co-Mn cathode with high stable cycling performance and storage stability via scalable continuous precipitation, Electrochim. Acta 291 (2018) 84–94. https://doi.org/10.1016/j.electacta.2018.08.124.

[48] N. Phattharasupakun, M. M. E. Cormier, E. Lyle, E. Zsoldos, A. Liu, C. Geng, Y. Liu, H. Li, M. Sawangphruk, J. R. Dahn, Correlating Cation Mixing with Li Kinetics: Electrochemical and Li Diffusion Measurements on Li-Deficient $LiNiO_2$ and Li-Excess

$LiNi_{0.5}Mn_{0.5}O_2$, J. Electrochem. Soc. 168 (2021) 090535. https://doi.org/10.1149/1945-7111/ac24ba.

[49] R.-C. Lee, J. Franklin, C. Tian, D. Nordlund, M. Doeff, R. Kostecki, The origin of impedance rise in Ni-Rich positive electrodes for lithium-ion batteries, J. Power Sources 498 (2021) 229885. https://doi.org/https://doi.org/10.1016/j.jpowsour.2021.229885.

[50] W. Zhao, L. Zou, H. Jia, J. Zheng, D. Wang, J. Song, C. Hong, R. Liu, W. Xu, Y. Yang, J. Xiao, C. Wang, J.-G. Zhang, Optimized Al Doping Improves Both Interphase Stability and Bulk Structural Integrity of Ni-Rich NMC Cathode Materials, ACS Appl. Energy Mater. 3 (2020) 3369–3377. https://doi.org/10.1021/acsaem.9b02372.

[51] C. Hong, Q. Leng, J. Zhu, S. Zheng, H. He, Y. Li, R. Liu, J. Wan, Y. Yang, Revealing the correlation between structural evolution and Li^+ diffusion kinetics of nickel-rich cathode materials in Li-ion batteries, J. Mater. Chem. A 8 (2020) 8540–8547. https://doi.org/10.1039/D0TA00555J.

[52] H.H. Ryu, N.Y. Park, T.C. Noh, G.C. Kang, F. Maglia, S.J. Kim, C.S. Yoon, Y.K. Sun, Microstrain Alleviation in High-Energy Ni-Rich NCMA Cathode for Long Battery Life, ACS Energy Lett. 6 (2021) 216–223. https://doi.org/10.1021/acsenergylett.0c02281.

[53] N.Y. Park, H.H. Ryu, G.T. Park, T.C. Noh, Y.K. Sun, Optimized Ni-Rich NCMA Cathode for Electric Vehicle Batteries, Adv. Energy Mater. 11 (2021). https://doi.org/10.1002/aenm.202003767.

Supporting Information

Slug-flow synthesis of NCMA: Effect of substitution of cobalt with aluminum on the electrochemical performance of Ni-rich cathode for lithium-ion battery

Arjun Patel[1], Sourav Mallick[1], Jethrine H. Mugumya[1], Nicolás Lopez-Riveira[1], Sunuk Kim[1], Mo Jiang[1], Mariappan Parans Paranthaman[2], Michael L. Rasche[1], Herman Lopez[3], and Ram B. Gupta[1]*

[1]*Department of Chemical and Life Science Engineering, Virginia Commonwealth University, Richmond, VA, 23219, USA.*

[2]*Chemical Sciences Division, Oak Ridge National Laboratory, Oak Ridge, TN, 37831, USA*

[3]*Ionblox Inc., Fremont, CA, 94538, USA*

Fig. S1. ICP-OES results for NCMA materials with different Cobalt and Aluminum content.

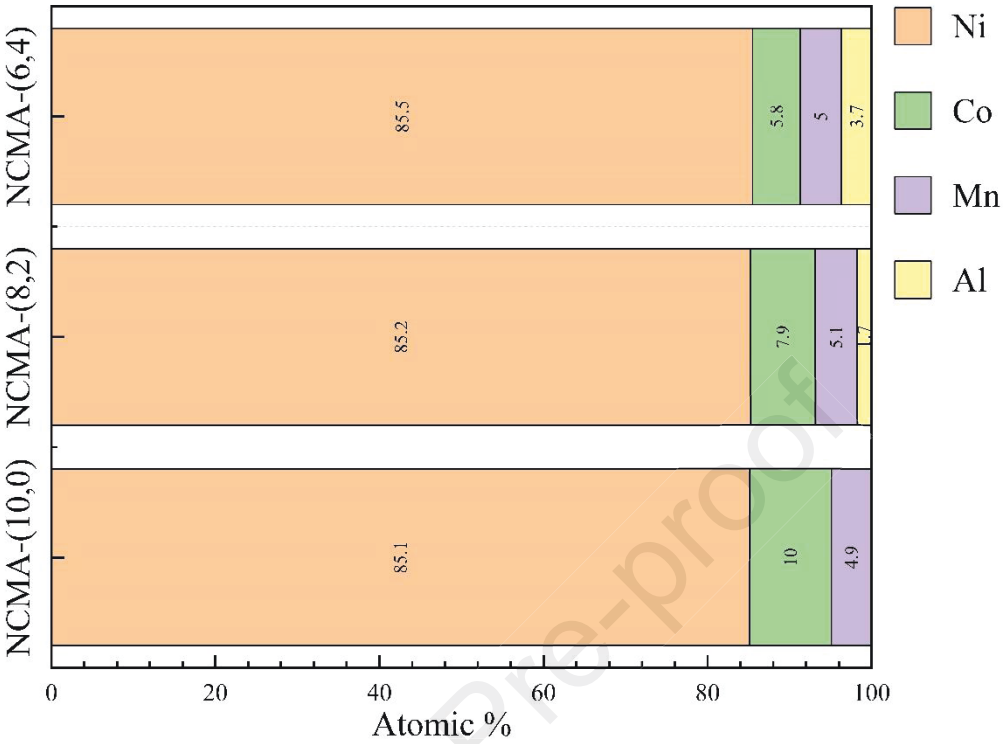

Fig. S2. EDX mapping of NCMA-oxalate (a) NCMA-(10,0), (b) NCMA-(8,2) and (c) NCMA-(6,4).

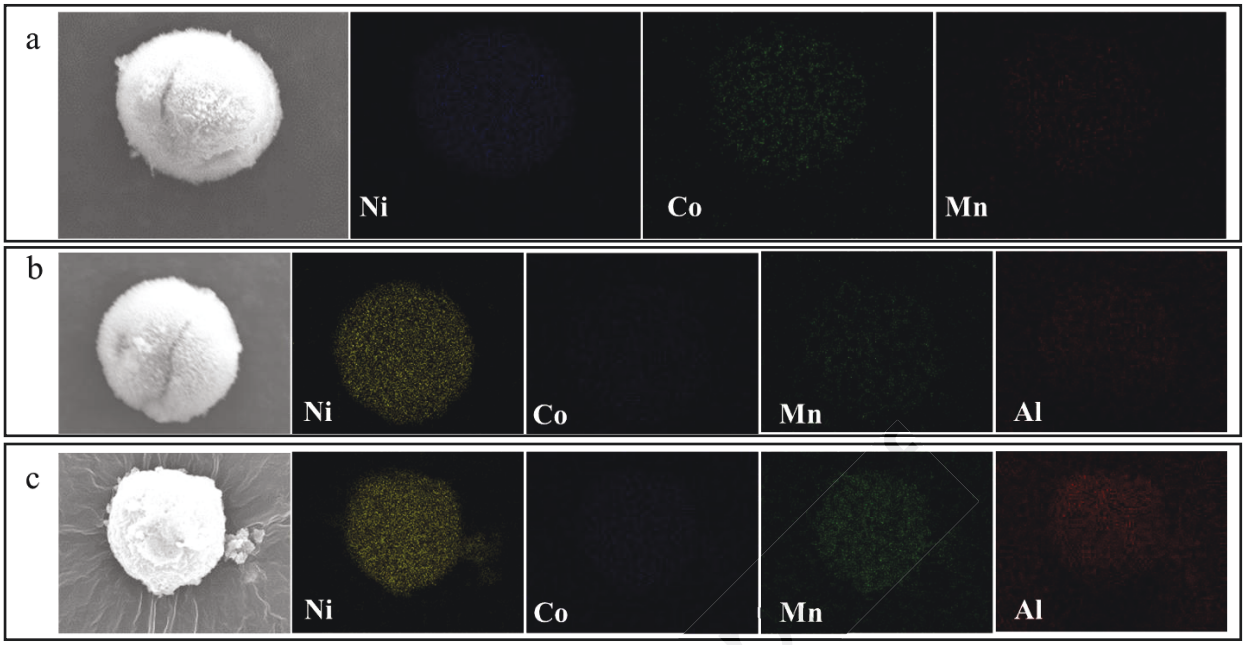

Fig. S3. SEM images with respect to feeding sequence (a) NH_4OH first followed by $(NH_4)_2C_2O_4$ and (b) $(NH_4)_2C_2O_4$ first followed by NH_4OH

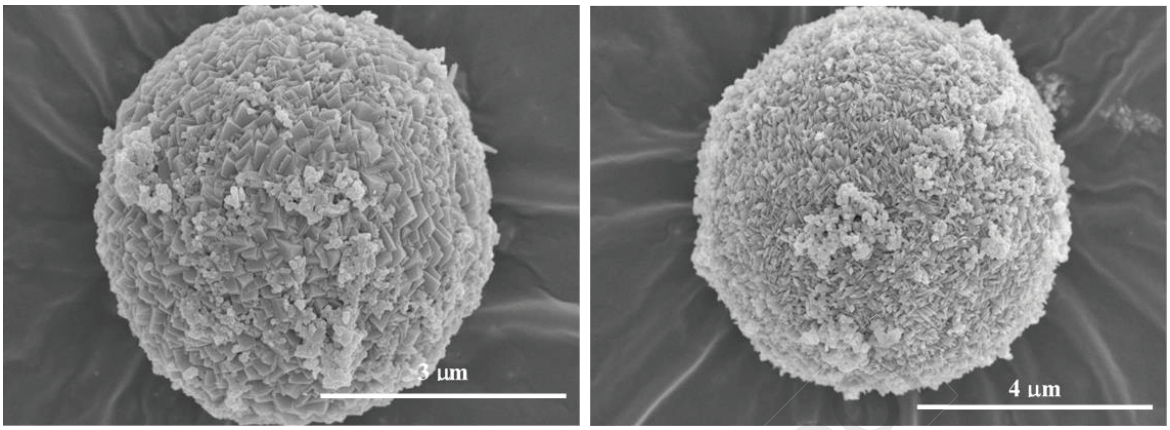

Fig. S4. TGA for NCMA-(10,0), NCMA-(8, 2) and NCMA-(6,4) in a) N_2 environment and b) Air environment

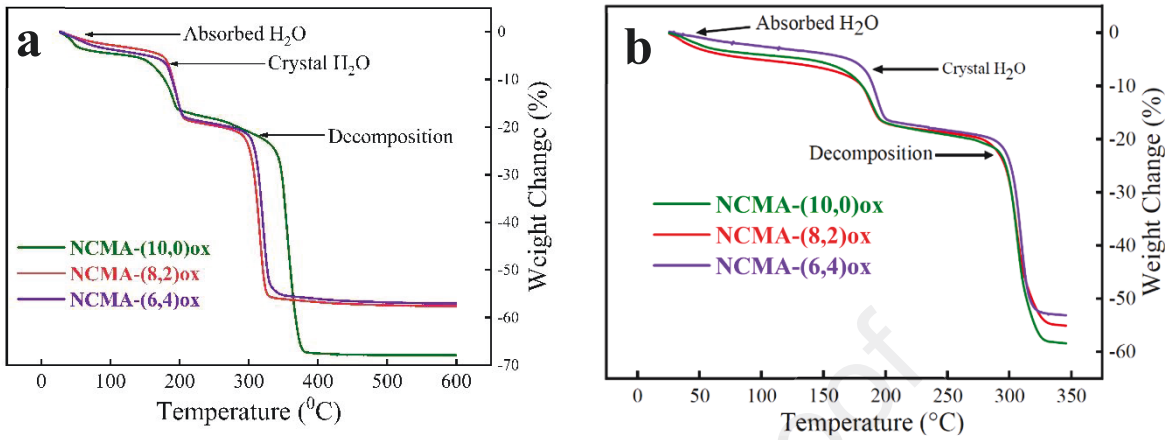

Fig. S5. The effect of higher heating rate (5 ^{0}C per min) during calcination.

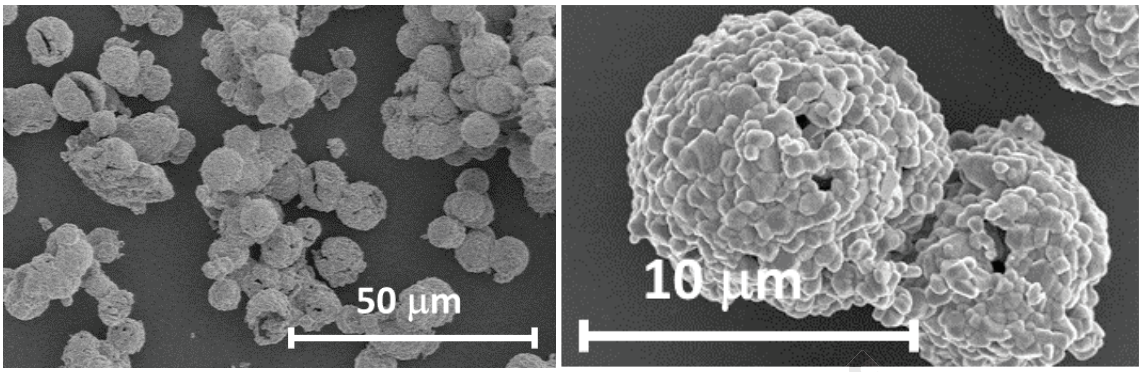

Fig. S6. Rietveld refinement of XRD profiles of (a) NCMA-(10,0), (b) NCMA-(8,2) and (c) NCMA-(6,4).

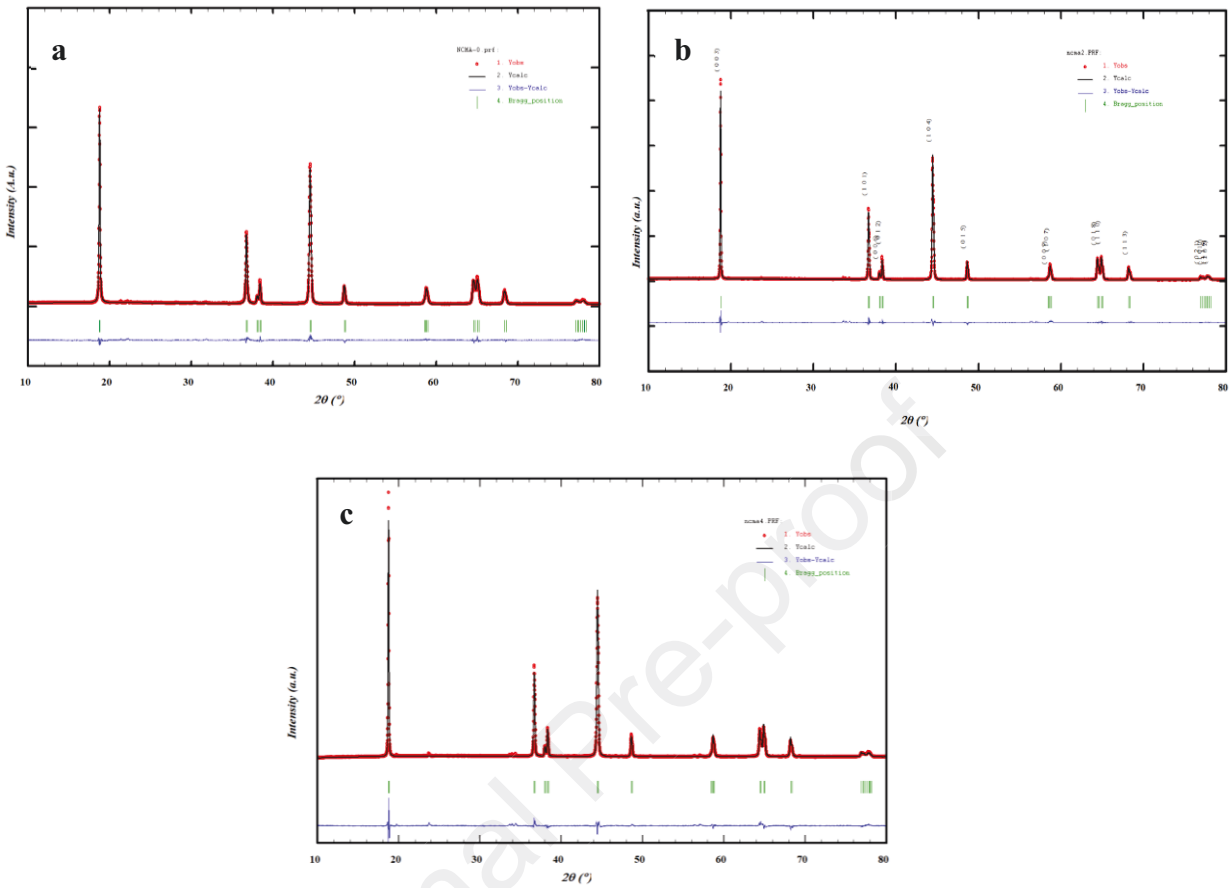

Fig. S7. Cross-sectional SEM images and EDX mapping profiles of (a) NCMA-(10,0), (b) NCMA-(8,2) and (c) NCMA-(6,4).

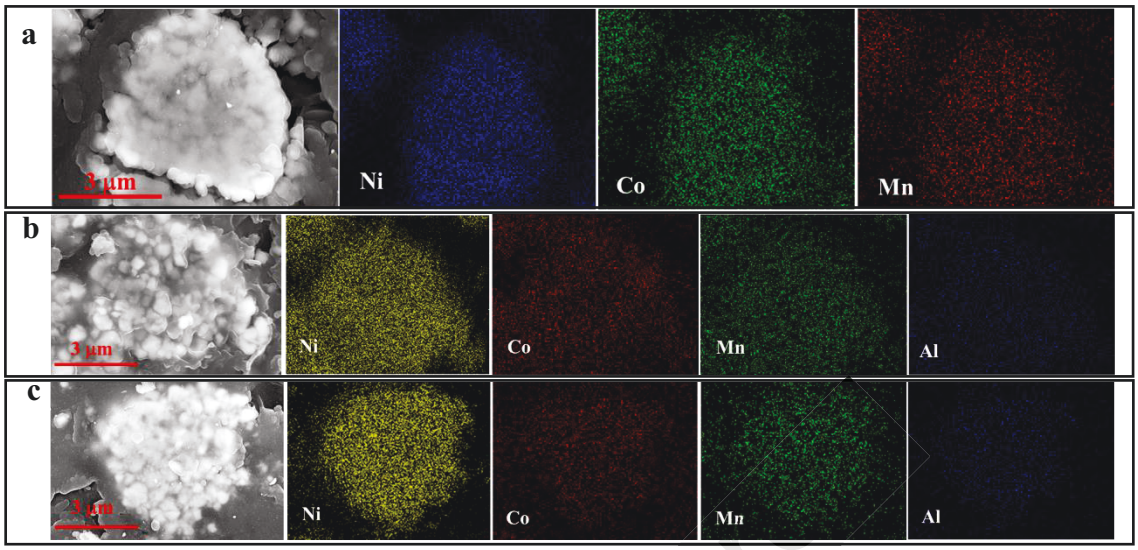

Fig. S8. Particle-size distribution profile of the three materials.

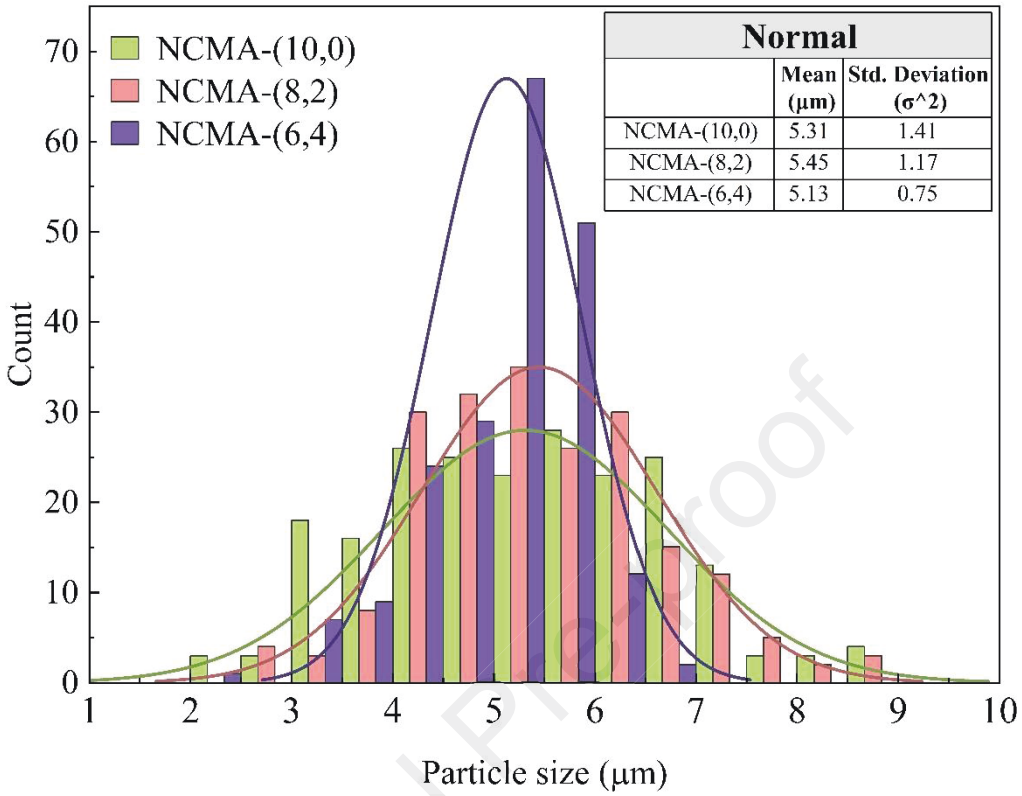

Normal	Mean (μm)	Std. Deviation (σ^2)
NCMA-(10,0)	5.31	1.41
NCMA-(8,2)	5.45	1.17
NCMA-(6,4)	5.13	0.75

Fig. S9. High-resolution profiles of (b) Ni 2p, (c) Co 2p, and (d) Mn 2p of NCMA-(10,0).

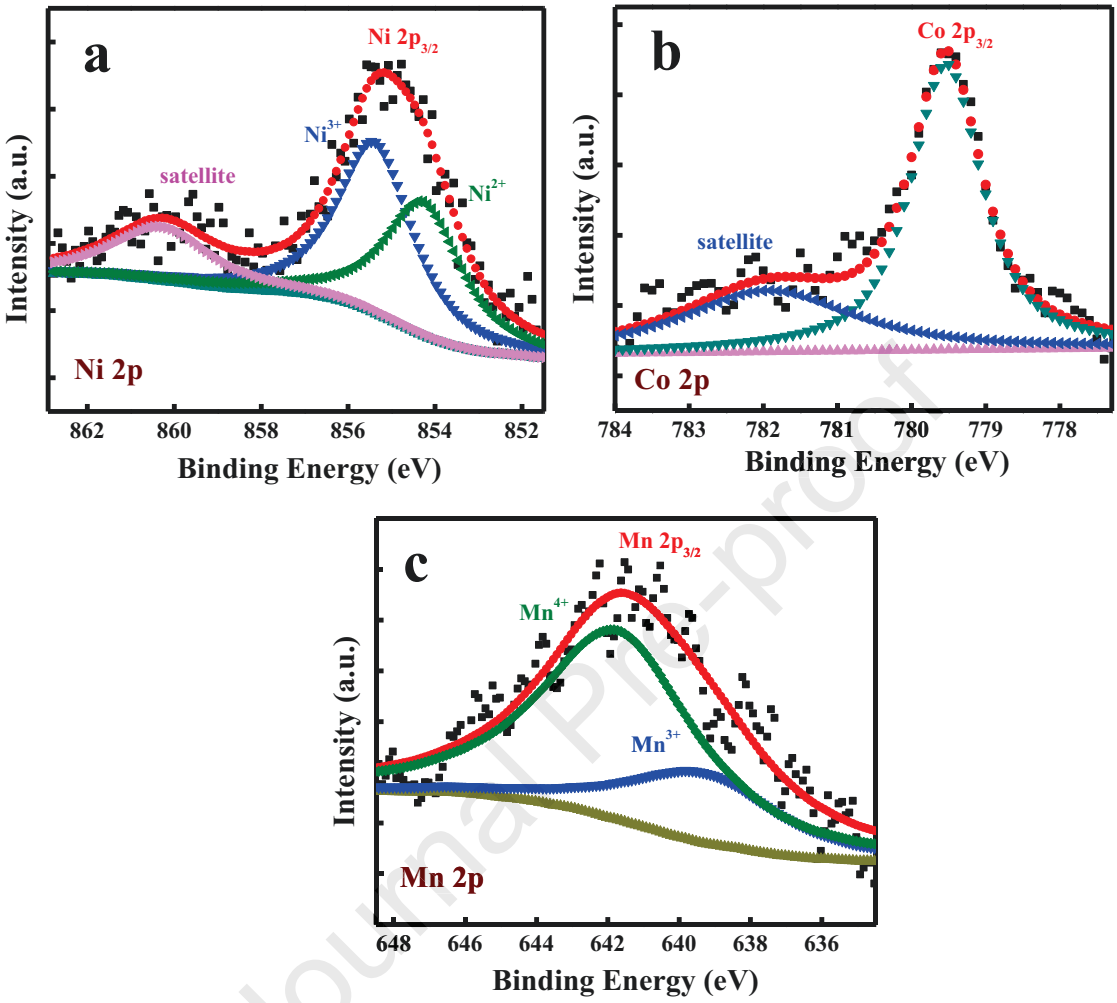

Fig. S10. Charge-discharge profile at different C-rates (a) NCMA-(10,0) (b) NCMA-(8,2) and (c) NCMA-(6,4).

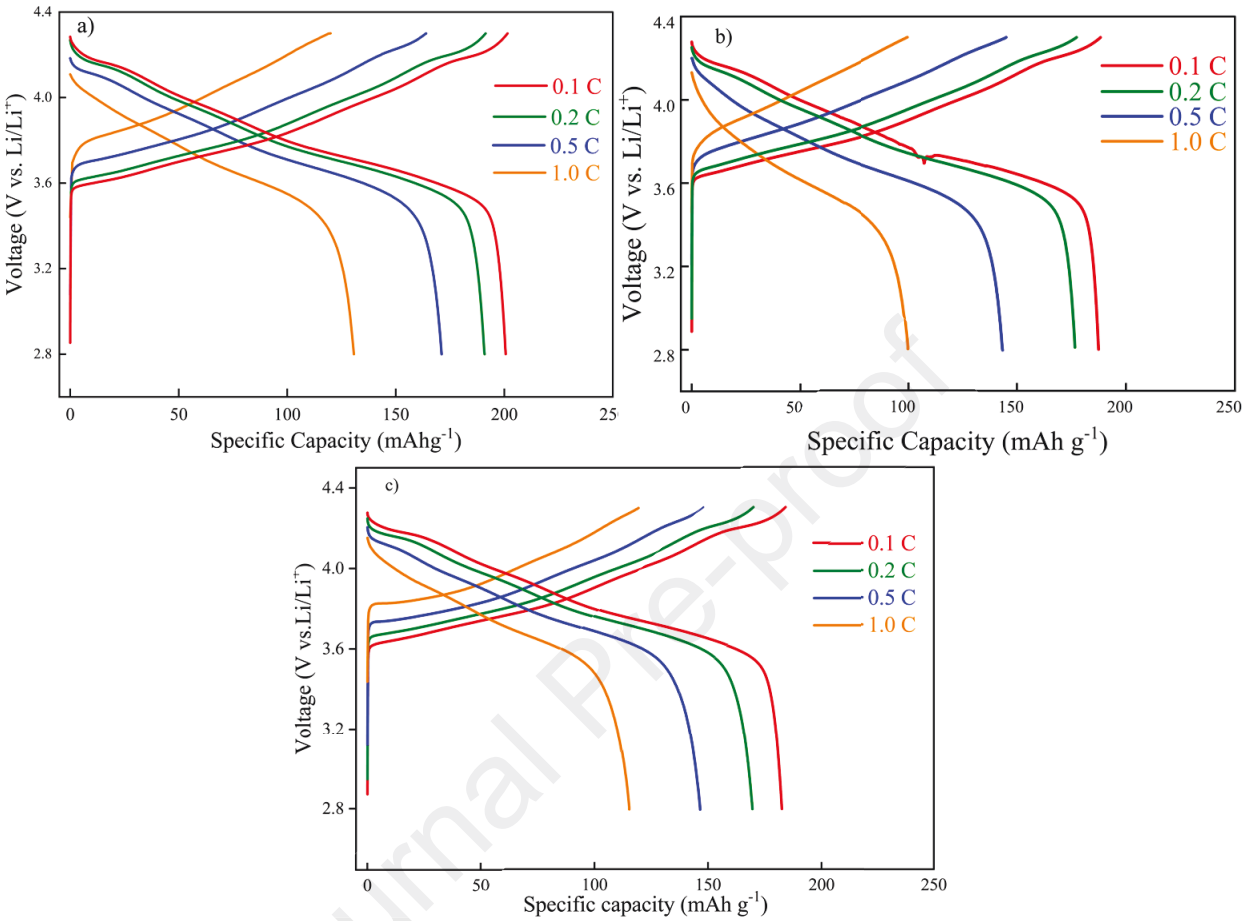

Fig. S11. First charge-discharge profiles for NCMA-(10,0), NCMA-(8,2) and (c) NCMA-(6,4) at 0.1 C

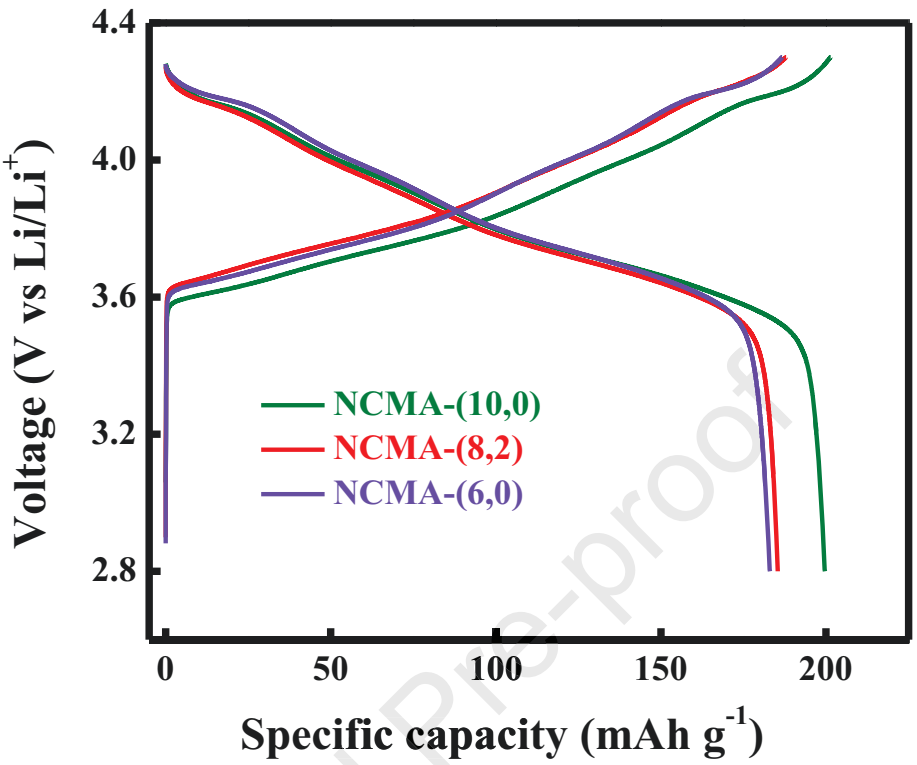

Table S1. Initial coulombic efficiency of the three materials.

Materials	Initial Coulombic efficiency (%)
NCMA-(10,0)	86.41
NCMA-(8,2)	80.42
NCMA-(6,4)	80

Fig. S12. Cycling profile of NCMA-(8,2) at 1 C in full cell configuration.

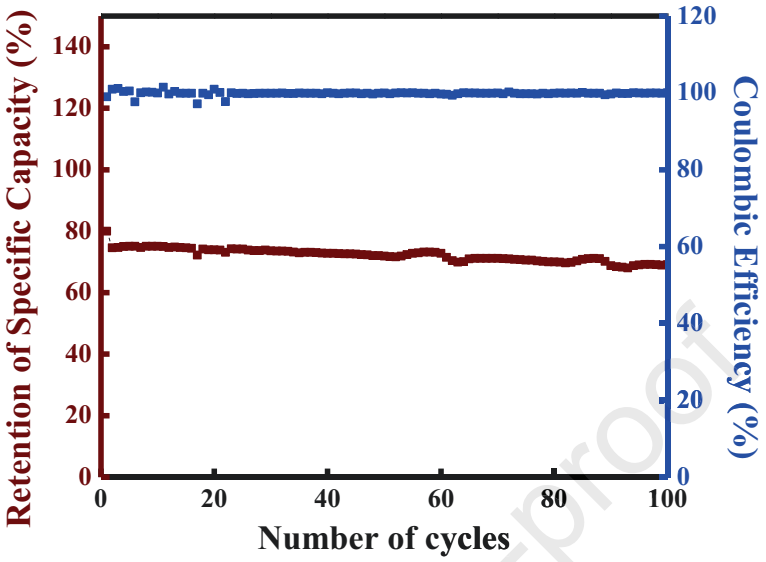

Fig. S13. Equivalent circuit and its various components

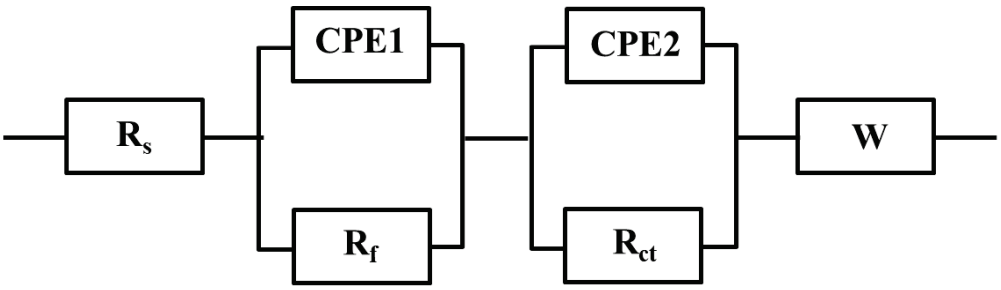

R_s = Solution resistance; R_f = surface resistance R_{ct} = charge-transfer resistance

CPE1 and CPE2 = Constant phase elements, associated with R_f and R_{ct}, respectively

W = Warburg impedance

The Li^+ diffusion co-efficient (D_{Li+}) is related with the Warburg component through the following equation:

$$D = R^2T^2(2A^2n^4F^4C^2\sigma^2)^{-1}$$

Where, R =gas constant; T= absolute temperature; A = area of the electrode; N= number of electrons transferred per molecule in the electrochemical reaction; F = Faraday constant; C = concentration of Li+ ions and σ = Warburg factor. The Warburg factor (σ) can be calculated from the slop of the Zre - ω-0.5 plot using the following relation.

Fig. S14. Cross-sectional SEM images of cycled cathodes (100 cycles) (a) NCMA-(10,0) and (b) NCMA-(8,2).

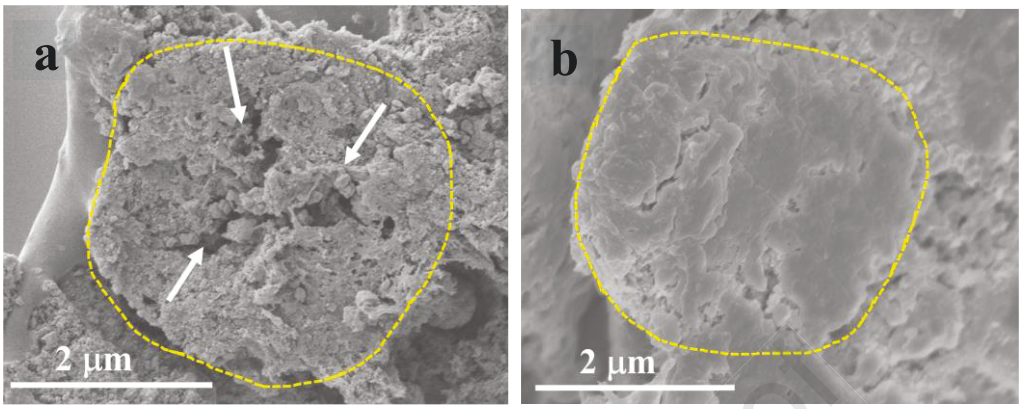

Fig. S15. Post-cycling (after 100 cycles) XRD profiles of (a) NCMA-(10,0) and (b) NCMA-(8,2).

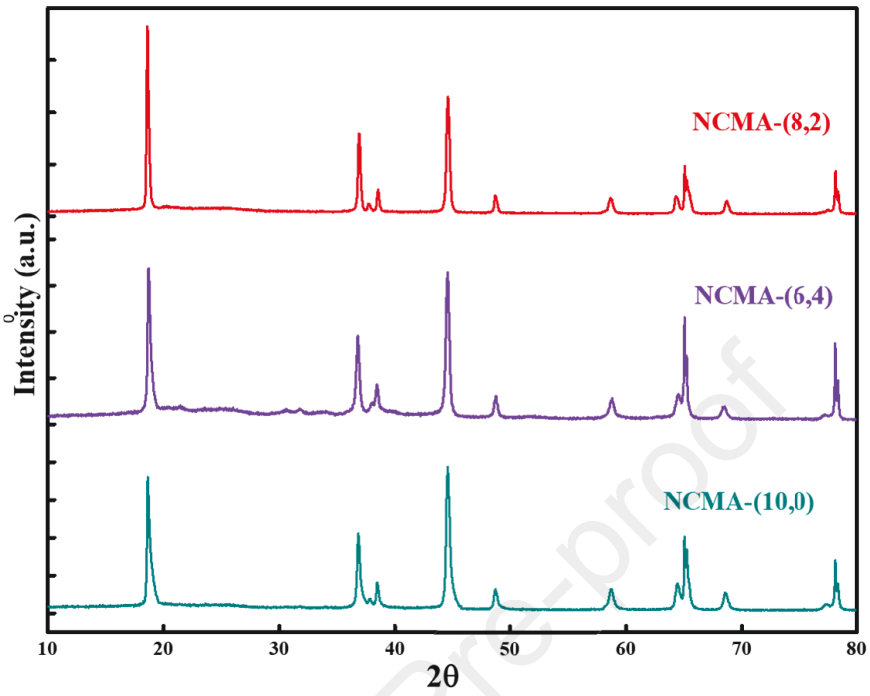

Table S2. Table based on the literature reports on Ni-rich NCM

S. No.	Material	Synthesis process	Voltage Window (V) (1C)	Specific Capacity (mAh g^{-1})	Cycling	Reference
1	(NCMA89) $Li[Ni_{0.89}Co_{0.05}Mn_{0.05}Al_{0.01}]O_2$	Co precipitation	2.7 – 4.3 (180 mAg^{-1})	228	90.66 % at 0.5 C after 100 cycles	[1]
2	(NCMA-4) $Li[Ni_{0.8}Co_{0.1}Mn_{0.06}Al_{0.04}]O_2$	Ultrasonic nebulizer	3.0-4.4 (180 mAg^{-1})	198	83.8% at 1C after 200 cycles	[2]
3	(NCM-Al 0.96%) $Li[(Ni_{0.4}Co_{0.2}Mn_{0.4})_0Al_{0.2}O_2{\cdot}20Ni_{0.83}Co_{0.12}Mn_{0.05}]O_2$	Co precipitation	2.8-4.5 (180 mAg^{-1})	195	83.8% at 1C after 200 cycles	[3]
4	(Al3-NCM) $Li[Ni_{0.894}Co_{0.041}Mn_{0.034}Al_{0.031}]O_2$	Co precipitation	2.7-4.3 (180 mAg^{-1})	220	86.00% at 1C after 100 cycles	[4]
5	$Li[Ni_{0.8}Co_{0.1}Mn_{0.1}]O_2$	Slug-flow Coprecipitation	2.8-4.3 (200 mAg^{-1})	202	62.00% at 0.1C after 50 cycles	[5]
6	$Li[Ni_{0.85}Co_{0.05}Mn_{0.10}]O_2$	Concentration gradient, coprecipitation	2.7-4.3 (180 mAg^{-1})	222	93.5% at 0.5 C after 100 cycles	[6]
7	$Li[Ni_{0.9}Co_{0.05}Mn_{0.05}]O_2$	Hybrid cathode Coprecipitation	2.7-4.3 (180 mAg^{-1})	228.7	92.2% at 0.5 C after 100 cycles	[7]
8	N-FCG-NCM811@LNO	Coprecipitation followed by7 Wet chemical method	3.0-4.4 (180 mAg^{-1})	214.8	85.1 at 1C after 300 Cycles	[8]
9	R-SC NCMA	Solvothermal method	2.8-4.3 (220 mAg^{-1})	226	95.6% at 5C after 100 cycles	[9]

10	$LiNi_{0.90}Co_{0.04}Mn_{0.03}Al_{0.03}O_2$	Coprecipitation	2.8-4.3 (200 mAg^{-1})	209	91.5 at 1C after 100 cycles	[10]

References

[1] U.H. Kim, L.Y. Kuo, P. Kaghazchi, C.S. Yoon, Y.K. Sun, Quaternary Layered Ni-Rich NCMA Cathode for Lithium-Ion Batteries, ACS Energy Lett. 4 (2019) 576–582. https://doi.org/10.1021/acsenergylett.8b02499.

[2] S. Wang, J. Zhu, Y. Li, G. Cao, Y. Chen, D. Zhang, Z. Tan, J. Yang, J. Zheng, H. Li, Role of Al on the electrochemical performances of quaternary nickel-rich cathode $LiNi_{0.8}Co_{0.1}Mn_{0.1-x}Al_xO_2$ ($0 \leq x \leq 0.06$) for lithium-ion batteries, J. Electroanal. Chem. 888 (2021). https://doi.org/10.1016/j.jelechem.2021.115200.

[3] Y. Han, X. Cheng, G. Zhao, W. Qiang, B. Huang, Effects of Al doping on the electrochemical performances of $LiNi_{0.83}Co_{0.12}Mn_{0.05}O_2$ prepared by coprecipitation, Ceram. Int. 47 (2021) 12104–12110. https://doi.org/10.1016/j.ceramint.2021.01.055.

[4] U.-H. Kim, S.-B. Lee, J.-H. Ryu, C.S. Yoon, Y.-K. Sun, Optimization of Ni-rich $Li[Ni_{0.92-x}Co_{0.04}Mn_{0.04}Al_x]O_2$ cathodes for high energy density lithium-ion batteries, J. Power Sources. 564 (2023) 232850. https://doi.org/10.1016/j.jpowsour.2023.232850.

[5] M. Mou, A. Patel, S. Mallick, K. Jayanthi, X.-G. Sun, M. Parans Paranthaman, S. Kothe, E. Baral, S. Saleh, J. H. Mugumya, M. L. Rasche, R. B. Gupta, H. Lopez, M. Jiang, Slug Flow Coprecipitation Synthesis of Uniformly-Sized Oxalate Precursor Microparticles for Improved Reproducibility and Tap Density of $Li(Ni_{0.8}Co_{0.1}Mn_{0.1})O_2$ Cathode Materials, ACS Appl. Energy Mater. 6 (2023) 3213–3224. https://doi.org/10.1021/acsaem.2c03563.

[6] C.S. Yoon, K.J. Park, U.H. Kim, K.H. Kang, H.H. Ryu, Y.K. Sun, High-Energy Ni-Rich $Li[Ni_xCo_yMn_{1-x-y}]O_2$ Cathodes via Compositional Partitioning for Next-Generation Electric Vehicles, Chem Mater. 29 (2017) 10436–10445. https://doi.org/10.1021/acs.chemmater.7b04047.

[7] U.H. Kim, H.H. Ryu, J.H. Kim, R. Mücke, P. Kaghazchi, C.S. Yoon, Y.K. Sun, Microstructure-Controlled Ni-Rich Cathode Material by Microscale Compositional Partition for Next-Generation Electric Vehicles, Adv. Energy Mater. 9 (2019). https://doi.org/10.1002/aenm.201803902.

[8] F. Zhao, X. Li, Y. Yan, M. Su, L. Liang, P. Nie, L. Hou, L. Chang, C. Yuan, A three-in-one engineering strategy to achieve $LiNi_{0.8}Co_{0.1}Mn_{0.1}O_2$ cathodes with enhanced high-voltage cycle stability and high-rate capacities towards lithium storage, J. Power Sources. 524 (2022). https://doi.org/10.1016/j.jpowsour.2022.231035.

[9] Z. Tao, G. Liu, S. Li, M. Yao, Y. Zhang, Rational structure of rod-like single crystal $LiNi_{0.9}Co_{0.05}Mn_{0.04}Al_{0.01}O_2$ cathode for superior-stable lithium-ion battery, Electrochim. Acta. 444 (2023). https://doi.org/10.1016/j.electacta.2023.141975.

[10] J. Jeyakumar, M. Seenivasan, Y.S. Wu, S.H. Wu, J.K. Chang, R. Jose, C.C. Yang, Preparation of long-term cycling stable ni-rich concentration-gradient NCMA cathode materials for li-ion batteries, J. Colloid. Interface Sci. 639 (2023) 145–159. https://doi.org/10.1016/j.jcis.2023.02.064.

Highlights

- Slug-flow continuous manufacturing technique is utilized to synthesize Al-doped Ni-rich LIB cathode
- Oxalate coprecipitation chemistry removes the issues of pH sensitivity and Mn oxidation
- Optimized Al-doping mitigate the issues of cation mixing and microcracking
- Co-substitution with Al efficiently improves the rate capability and cycling performance of the Ni-rich cathode

Declaration of interests

☒ The authors declare that they have no known competing financial interests or personal relationships that could have appeared to influence the work reported in this paper.

☐ The authors declare the following financial interests/personal relationships which may be considered as potential competing interests: